A Cross Section of Oscillator Dynamics

by

Jason A. De Salvo

M.S. Electrical Engineering, 2004

University of Colorado at Boulder

A thesis submitted to the

Faculty of the Graduate School of the

University of Colorado in partial fulfillment

of the requirements for the degree of

Master of Science

Department of Applied Math

2010

This thesis entitled:
A Cross Section of Oscillator Dynamics
written by Jason A. De Salvo
has been approved for the Department of Applied Math

James Meiss

James Curry

Juan Restrepo

Date

The final copy of this thesis has been examined by the signatories, and we find that both the content and the form meet acceptable presentation standards of scholarly work in the above mentioned discipline.

De Salvo, Jason A. (Applied Mathematics)

A Cross Section of Oscillator Dynamics

Thesis directed by Professor James Meiss

The goal of this research is to explore criteria sufficient to produce oscillations, sample some dynamical systems that oscillate, and investigate synchronization. A discussion on linear oscillators attempts to demonstrate why autonomous oscillators are inherently nonlinear in nature. After describing some criteria on second-order dynamics that ensure periodic orbits, we explore the dynamics of two second-order oscillators in both autonomous and periodically driven fashion. Finally, we investigate the phenomena of synchronization with the nonlinear phase-locked loop. Methods of analysis are exemplified as they become relevant including Poincaré maps and the Zero-One test for chaos.

The Poincaré-Bendixson theorem is used to demonstrate the existence of periodic orbits in $\mathbb{R}^2$ under extraordinarily general conditions. Liénard's equation and theorem are introduced, which provide an intuitive parameterization for a class of oscillators. Liénard's equation is a second-order, ordinary differential equation that characterizes an oscillator with respect a state dependent damping function and a restoring force function. Liénard's theorem establishes sufficient criteria under which the Liénard's equation has a unique, stable, limit cycle.

The Duffing equation conforms with the Liénard equation, yet produces limit cycles without satifying Liénard's theorem. Our Duffing dynamics are explained in the context of a nonlinear spring model. We survey the parameter space, which form both pitchfork and hyperbolic potential wells with respect to the displacement. These two wells characterize the bifurcations between the four fundamental undamped dynamical modes. One interesting result is that chaotic trajectories of the Duffing equation are able to quickly shed light on a multitude of quasi-periodic trajectories at the boundaries of the Poincaré map.

Next we introduce an oscillator that is similar to many engineered oscillators. The Van der

Pol (VDP) oscillator model is presented in the context of a nonlinear current source in parallel with an inductor, a capacitor, and a resistor. It provides a net negative conductance destabilizing the equilibrium, and is tamed into global stability by increasing damping by the square of the voltage. The VDP oscillator is the opposite of the Duffing equation in that its nonlinearity is in the damping function, with a linear restoring force function. Like the VDP oscillator, many engineered oscillators are self-excited, autonomous systems that produce limit cycles.

Finally, we investigate the process of synchronization with the phase-locked loop (PLL). Synchronization is a nonlinear process in which systems entrain their frequencies to external signals or other systems. Naturally occurring PLLs lie at the foundation of synchronization. We describe the basic topology of the PLL. Interestingly, the phase model introduced conforms with Liénard's equation and is similar to the model used for the Josephson junction and the driven pendulum. Perhaps explaining the prevalence of synchronization, we show that almost any nonlinear functional can serve as a phase detector. We briefly demonstrate a phase-lock of two oscillators with phase-noise analysis. Finally, we report on the nonlinear behavior of the PLL when subjected to a modulated input.

Acknowledgements

Thanks to Professor James Meiss for sharing his knowledge and interest in nonlinear dynamics.

Contents

Chapter

Tables

Table

Figures

Figure

Chapter 1

Oscillator Dynamics

1.1 Introduction

We are interested in a subset of dynamical systems that are capable of sustained oscillations. Of course, at a quantum level, all matter exhibits oscillations. In this chapter, we narrow the types of systems under study and look at some criteria sufficient for second-order systems to achieve periodic orbits. The three most common classifications of oscillators are harmonic (resonant) oscillators, limit-cycle oscillators, and delayed-feedback oscillators. Resonant systems release stored energy within narrow frequency bandwidths. In the next chapter we explore a particularly interesting nonlinear resonator with the Duffing Equation. Limit-cycle oscillators rely on nonlinear attractors to constrain an orbit to a region without any stable equilibrium points. We present a classic example of this in Chapter 3 with the Van der Pol oscillator. Finally, we investigate a process by which oscillating systems become synchronized using the phase-locked loop in Chapter 4.

1.2 General Dynamics Model

We describe a system's dynamics in terms of a flow of states in time. Let $x(t) \in \mathbb{R}^n$ be a time dependent vector of n states which characterize the system of interest. To simplify concerns over the existence and uniqueness of solutions to dynamical systems, we limit our scope of interest to real continuous systems that can be described with a differentiable vector field

$$\dot{x} = f(x,t), \quad x(t_o) = x_o \tag{1.1}$$

$$f \in C^1 : \mathbb{R}^{n+1} \rightarrow \mathbb{R}^n$$

where $\dot{x}$ is the time derivative of x and we suppress explicit time dependence, $x(t) \rightarrow x$. Here the state flow can be thought of as the integral of the vector field, $f(x,t)$, beginning at a one-sided boundary condition $x(t_o) = x_o$. It is also possible to re-formulate (1.1) in an autonomous form $\dot{x} = f(x)$ by incorporating elapsed time into the state vector when desirable.

1.3 Numerical Integration Technique

Experience demonstrates that the flow will rarely be solvable in closed form; so, we incorporate numerical integration techniques to simulate the flow using computers. The 32-bit computing environment chosen incorporates a C/C++ compiled vector field model, conveniently driven by Matlab/Simulink®via S-functions. We utilize the Dormand-Prince[1] method, which is a Runge-Kutta(4,5), one-step, ODE solver. This method computes fourth order solutions with an error estimated from the fifth order solution. It proves to be computationally efficient for non-stiff, ordinary differential equations when attempting to achieve moderate accuracy. The flow for all examples simulated were required to meet an absolute tolerance of 10^{-8}, and relative tolerance of 10^{-6}.

1.4 Periodic Orbits from Linear Dynamics

In this section we will describe the second-order, simple harmonic oscillator model, review the conditions under which linear systems generate periodic orbits, and demonstrate that the center subspace is impractically narrow to accommodate realizable oscillators.

Linearizing about equilibria is one of the first natural steps taken when analyzing a nonlinear system. In addition to understanding the local behavior at the point of linearization, insight into system dynamics can be gained from frequency analysis methods. In science and engineering we often approximate oscillator dynamics as linear systems that generate periodic orbits. Under these conditions (1.1) is readily solvable. When projected onto a line, these trajectories are represented

by sinusoidal solutions. The familiarity of sinusoids provides a base for which to understand general oscillators, sometimes at the exclusion of better techniques. For instance, linearized systems are ineffectual in understanding fundamental bifurcations in realizable oscillators.

1.4.1 Simple Harmonic Oscillator

A useful point of reference is the second-order, simple harmonic oscillator, described here with a forcing input $u(t)$.

$$\ddot{x} + 2\zeta\omega_n\dot{x} + \omega_n^2 x = u(t) \tag{1.2}$$

This ubiquitous parameterization describes a system in terms of a damping coefficient, ζ, and a natural frequency, ω_n. A high-order, nonlinear system may be described locally by a linearization that captures the dynamics about a trajectory. Although the linearization may be more complex than (1.2), one can often capture the fundamental properties of interest by the dominant second-order eigenvalues. Basic understanding of the second-order, simple harmonic oscillator can be found in linear systems texts. We will make reference to this model when comparing nonlinear models developed later.

1.4.2 Space of Linear Oscillators

Consider the following first-order, linear, time-invariant system described by matrix $A \in \mathbb{R}^{n\times n}$:

$$\dot{x} = Ax, \quad x(0) = x_o. \tag{1.3}$$

This form is general enough to include time-invariant linear dynamics of any order. In the absence of a forcing function, the vector field has no time dependence and the rate of change of any state is a linear combination of the current states.

Linear dynamic systems are readily solved through the formulation of the matrix exponential. Pertinent to our interest in characterizing oscillator dynamics, we recall that linear dynamics can

be trifurcated into unstable, center, and stable subspaces. These subspaces can be distinguished directly by decomposing A into it's semisimple and nilpotent parts.

Theorem 1 (Spectral Decomposition) A matrix A on a complex vector space E, has a unique decomposition, $A = S + N$, where S is semisimple, N is nilpotent, and $SN - NS = 0$. (See Meiss, 2007, Thm 2.8 for the proof.[2])

Define the diagonalization of S by

$$P^{-1}SP = \Lambda = diag(\lambda_1, \ldots, \lambda_n)$$

Using the commutative aspects of S and N, and some properties of the matrix exponential expansion, we have

$$e^{At} = e^{St}e^{Nt} = Pe^{\Lambda t}P^{-1}\left(\sum_{j=0}^{n-1}\frac{(Nt)^j}{j!}\right) \tag{1.4}$$

Note that the spectral stability is determined by the real part of the eigenvalues found in the diagonal of Λ. The center subspace is narrowly defined as the span of the generalized eigenspace associated with eigenvalues with zero real part. Consider an eigenvector v_k associated with an eigenvalue λ_k of algebraic multiplicity n_k. Then the center subspace is

$$\{\text{Span}(v_k) \,:\, (A - \lambda_k I)^{n_k} v = 0, \text{ where } Real(\lambda_k) = 0\}$$

Linear oscillators can exist within the center subspace. Most observable systems have irreversible processes (entropy) and are not Hamiltonian. It is probabilistically unlikely that a system will have eigenvalues that are exactly zero, and even if it should, equation (1.4) demonstrates that complex conjugate eigenvalues with zero real part are not guaranteed to generate a limit cycle when $n_k > 1$, as the stability is affected by the nilpotent part of A.

As a consequence of this narrowly defined space, autonomous oscillators are inherently nonlinear systems. At times, engineers and mathematicians utilize linear techniques to approximate

an autonomous oscillator's dynamics through time-varying models that allow the dominant poles to periodically transition about the center subspace. The stability of these periodic models can be studied by means of the monodromy matrix. Because neither time-invariant or time-varying linear analysis is effectual in understanding the fundamental bifurcations of nonlinear systems, we will not focus on them. Instead, we will utilize numerical simulation and visual aids to analyze oscillator dynamics.

1.5 The Existence of Oscillators

1.5.1 Defining a Limit Cycle

We define the forward orbit and reverse orbit of a system flow $\phi_t(x)$, starting from x at $t = 0$ as

$$\Gamma_x^+ = \{\phi_t(x) : t \in \mathbb{R}^+\}, \quad \Gamma_x^- = \{\phi_t(x) : t \in \mathbb{R}^-\}$$

A limit point of a forward orbit is a point y such that $\phi_{t_k}(x) \to y$ as $t_k \to \infty$ for some sequence $t_1 < t_2 < \cdots < t_k$. By the Bolzano-Weierstrass Theorem, we know that any sequence contained in a compact set has at least one limit point.

Define the ω-limit set and α-limit set as the set of all forward/reverse limit points of the flow from x.

$$\omega(x) = \{y : \lim_{k\to\infty} \phi_{t_k}(x) \to y, \text{ for any strictly increasing } \{t_k\} \to \infty\}$$

$$\alpha(x) = \{y : \lim_{k\to\infty} \phi_{t_k}(x) \to y, \text{ for any strictly decreasing } \{t_k\} \to -\infty\}$$

To reduce redundancy, we will focus on characterizing forward orbits only. It can be shown[2] that the ω-limit set is closed and invariant. Moreover, when Γ_x^+ is contained in a compact set, then $\omega(\Gamma_x)$ is nonempty, compact, and connected.

Now we can define a **limit cycle** as a closed, invariant, periodic orbit γ approached by the limit set of some other orbit. For example, a forward limit cycle, γ, exists for the orbit from x, if $\exists\ T \in \mathbb{R}^+$ such that

$$\{\gamma(t) : t \in \mathbb{R}\} = \omega(x) \text{ where } x \notin \gamma, \text{ and } \gamma(t + kT) = \gamma(t)\ \forall k \in \mathbb{N}^+$$

Although occasionally, the term "oscillator" is used in reference to systems with stable, non-periodic, or even chaotic orbits; generally, it is reserved for systems that exhibit periodic orbits or limit cycles. Sometimes quasi-periodic systems are filtered to produce periodic orbits, so the underlying oscillator is actually quasi-periodic. Note that a Lyapunov stable forward orbit defines a compact sequence and the Bolzano-Weierstrass Theorem ensures any sequence contained in a

compact set has at least one limit point; however, there is no assurance of periodicity for n-dimensional dynamic systems. Remarkably, with second-order dynamics, fairly mild conditions ensure that a system will have simple periodic orbits.

1.5.2 General Second-Order Periodic Orbits

By contrast to the lack of realizable linear oscillators, periodic orbits are one of the few options of second-order nonlinear systems. Under the following criteria, the only possible ω-limit sets are periodic orbits.

Theorem 2 (Poincaré-Bendixson Criterion) Given an autonomous second-order system

$$\dot{x} = f(x) \tag{1.5}$$

where $f(x)$ is continuously differentiable. Let M be a closed bounded subset of $\mathbb{R}^2$. If

(1) M contains no equilibrium points of (1.5), or contains only one equilibrium point with positive real eigenvalues; and,

(2) Every trajectory of (1.5) starting in M stays in M for all future time.

Then M contains a periodic orbit of (1.5). We refer to proofs in [2][3].

This theorem narrows the dynamic possibilities of a vast set of globally stable systems to simple periodic orbits. Specifically, it is eliminating the possibility of quasi-periodic or chaotic trajectories in unforced, stable, second-order systems with continuously differentiable vector fields.

1.5.3 Liénard's Second-Order Oscillator Model

Liénard's equation, written here, provides a flexible second-order model with an intuitive parameterization:

$$\ddot{x} + f_\delta(x)\dot{x} + g_\omega(x) = 0 \tag{1.6}$$

The function g_ω is a restoring force, which has a strong influence on an oscillator's frequency when not excessively damped; we indicate with "ω" that g_ω determines the natural angular frequency. The function f_δ is the damping force which contributes to the shape of the oscillator's output, $x(t)$. Following Meiss[2], we make use of the nonstandard change of variables $y = \dot{x} + F_\delta(x)$, where $F_\delta(x) = \int_0^x f_\delta(z)\,dz$, to formulate the first-order equivalent system

$$\dot{x} = y - F_\delta(x) \tag{1.7}$$

$$\dot{y} = -g_\omega(x) \tag{1.8}$$

In 1928, Liénard studied this system and provided the following sufficient conditions for periodic orbits in second-order, dynamic systems.

Theorem 3 (Liénard's Theorem) Liénard's equation (1.6), produces a unique, periodic orbit under the following conditions:

(i) F_δ and g_ω are odd, so that $F_\delta(0) = g_\omega(0) = 0$;

(ii) $xg_\omega(x) > 0$ for $x \neq 0$;

(iii) a is the unique positive zero of F_δ, and $F_\delta(x) < 0$ for $x \in (0, a)$;

(iv) $F_\delta(x)$ increases monotonically for $x > a$;

(v) $F_\delta(x) \to \pm\infty$ as $x \to \pm\infty$

This theorem, although significantly less general than the Poincaré-Bendixson Criterion, provides a lot more guidance when analyzing a large class of oscillators. These oscillators need a standard restoring force, $g_\omega(x)$, in the neighborhood of the equilibrium point such as would exist in a harmonic oscillator. The damping force, f_δ, is required to both destabilize the neighborhood about the equilibrium point with negative damping, while also providing global stability by retaining positive damping beyond a fixed displacement, $x = a$.

Note that neither the Poincaré-Bendixson Criterion, nor Liénard's Theorem can be generalized to higher dimensions or non-autonomous systems. We shall see that introducing a non-autonomous input to Liénard's equation can give rise to chaotic solutions.

1.5.4 Energy Dissipation in Liénard's Oscillator

Noting that y and $g_\omega(x)$ are proportional to the momentum and restorative force. The total energy in Liénard's Oscillator is

$$H(x,y) = \frac{1}{2}y^2 + \int_0^x g_\omega(z)\,dz$$

In general, energy decays/grows at a rate of

$$\frac{dH}{dt} = \frac{\partial H}{\partial x}\dot{x} + \frac{\partial H}{\partial y}\dot{y} = -g_\omega(x)F_\delta(x)$$

When there is no damping term, $f_\delta(x) \equiv 0$, Liénard's equation produces a second-order Hamiltonian oscillator.

Chapter 2

The Duffing Equation

2.1 Motivation

The Duffing equation was studied by G. Duffing in 1918 with respect to a nonlinear spring model. A linear spring produces a force in proportion to a displacement (input); naturally spring model counterparts abound in applied mathematics. The key feature explored by Duffing's model is that the linear range is often limited in real systems by nonlinear effects. Specifically, his equation places a nonlinearity in the restoring force, g_ω, of Liénard's equation (1.6) that causes a stiffening or softening of the spring constant at high displacements.

We choose to put an emphasis on the Duffing equation because it is becoming more important to oscillators of the future. As oscillators become smaller and higher in frequency, the scale of the resonators necessarily become microscopic. These microscopic resonators, such as quartz crystals, are effectively vibrating nonlinear springs that saturate with the smallest conceivable input signal. This causes an inherent Duffing effect.

2.2 Nonlinear Spring Model

Here is the Duffing equation:

$$\ddot{x} + 2\gamma\dot{x} + (\alpha + \beta x^2)x = u(t) \tag{2.1}$$

In spring model terminology, x represents the displacement from equilibrium, while γ, α and β are parameters that describe the damping, spring constant, and nonlinear effect respectively. Note that

unlike a physical spring, we allow the spring constant, α, to be negative ensuring an unstable focus at $(\dot{x}, x) = (0, 0)$. We will study a few parameterizations and the inclusion of a periodic forcing term $u(t)$.

One reason that the Duffing equation is popular in academia is that it is one term away from being the characteristic linear second-order dynamical system, yet, as we will see, it can exhibit quasi-periodic and chaotic behavior when pumped at different frequencies. The only nonlinear term is the force caused by βx^3. This force remains negligible for small displacements but can suddenly overpower the linear restoring force as displacement increases. That effect is a stiffening or softening as β ranges from positive to negative.

2.3 Potential Well Bifurcations

We will describe the dynamic variations possible in the unforced Duffing model. By isolating $\ddot{x}$ on the left hand side of Duffing's equation, the right hand side becomes proportional to the force driving the system. Ignoring external inputs, that force is equal to $-2\gamma\dot{x} - \alpha x - \beta x^3$. For $(\gamma, \beta) = (0, 0.3)$, we plot this force in Figure 2.1a as a function of α and x. This type of transition is aptly known as a pitchfork potential well. Similarly, Figure 2.1b shows the hyperbolic potential well for $(\gamma, \alpha) = (0, 0.3)$, as a function of β and x. Notice that as β becomes negative, adjacent equilibrium potentials are introduced at $x = \pm\infty$ as a hyperbolic function of β.

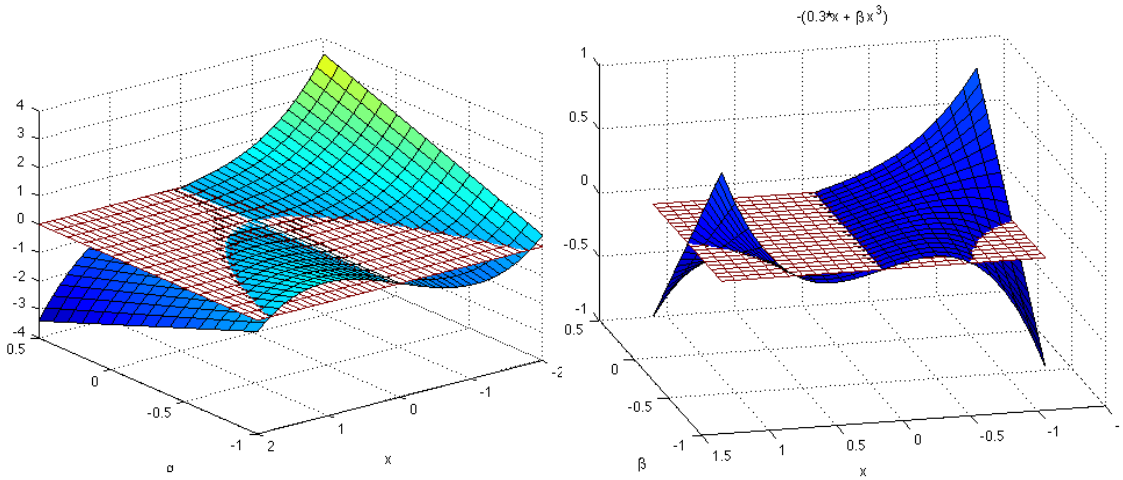

a) Pitchfork Well, $-(\alpha x + 0.3x^3)$ b) Hyperbolic Well, $-(0.3x + \beta x^3)$

Figure 2.1: Potential Wells of Duffing Equation

Converting (2.1) to first-order form with $x_1 = x$, and $x_2 = \dot{x}$

$$\dot{x}_1 = x_2$$

$$\dot{x}_2 = -2\gamma x_2 - x_1(\alpha + \beta x_1^2) + u(t)$$

The equilibrium points occur when $x_2 = 0$ and $x_1^2 = \{0, -\alpha/\beta\}$.

The four phase plots at the corners of Figure 2.2 encompass the undamped modes possible in the Duffing equation. All the equilibria found are either centers or unstable foci. The non-corner plots demonstrate how these modes transition from one to another. The right hand column shows the hyperbolic bifurcation associated with Figure 2.1b. Across the top row of Figure 2.2, where $\beta = 0.3$, we have the parabolic bifurcation associated with the pitchfork well in Figure 2.1a. Figure 2.3 shows how damping, $\gamma > 0$, causes the forward flow to decay toward stable equilibria. This lack of limit-cycles indicates that no parameterization isolates energy from the dissipative effect of γ.

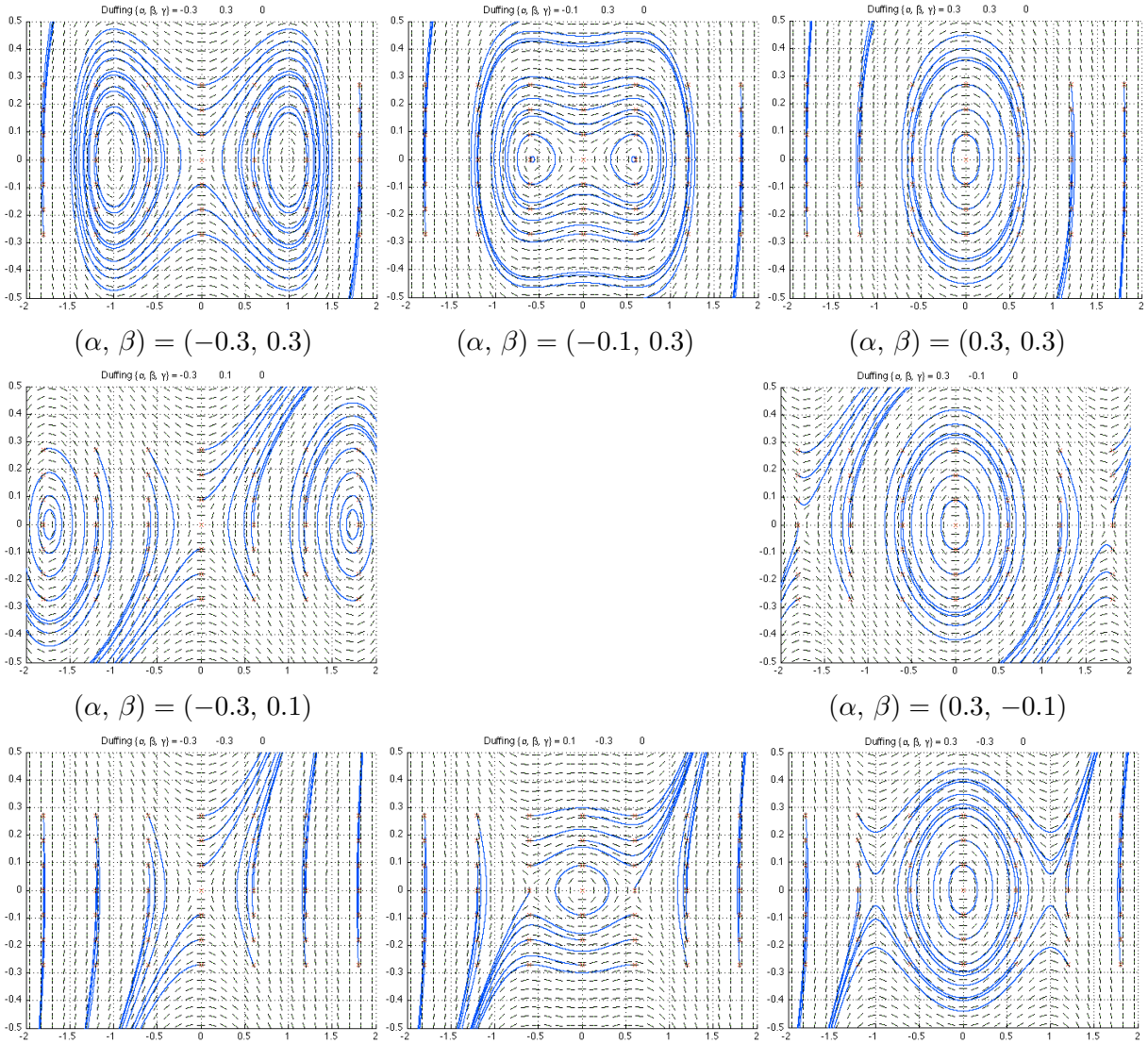

$(\alpha,\ \beta) = (-0.3,\ 0.3)$ $(\alpha,\ \beta) = (-0.1,\ 0.3)$ $(\alpha,\ \beta) = (0.3,\ 0.3)$

$(\alpha,\ \beta) = (-0.3,\ 0.1)$ $(\alpha,\ \beta) = (0.3,\ -0.1)$

$(\alpha,\ \beta) = (-0.3,\ -0.3)$ $(\alpha,\ \beta) = (0.1,\ -0.3)$ $(\alpha,\ \beta) = (0.3,\ -0.3)$

Figure 2.2: Duffing Phase Plane Plots, $\gamma = 0$

2.4 Forced Duffing Dynamics

As with all linear differential equations, when the Duffing equation is made linear by setting $\beta = 0$, the solution space can be described as the superposition of forced and transient dynamics. Moreover, the steady-state solution will be magnitude and phase shifted according to the forcing spectra. However, the invalidity of superposition in nonlinear differential equations leads to steady-state solutions with spectra not accounted for in the forcing function.

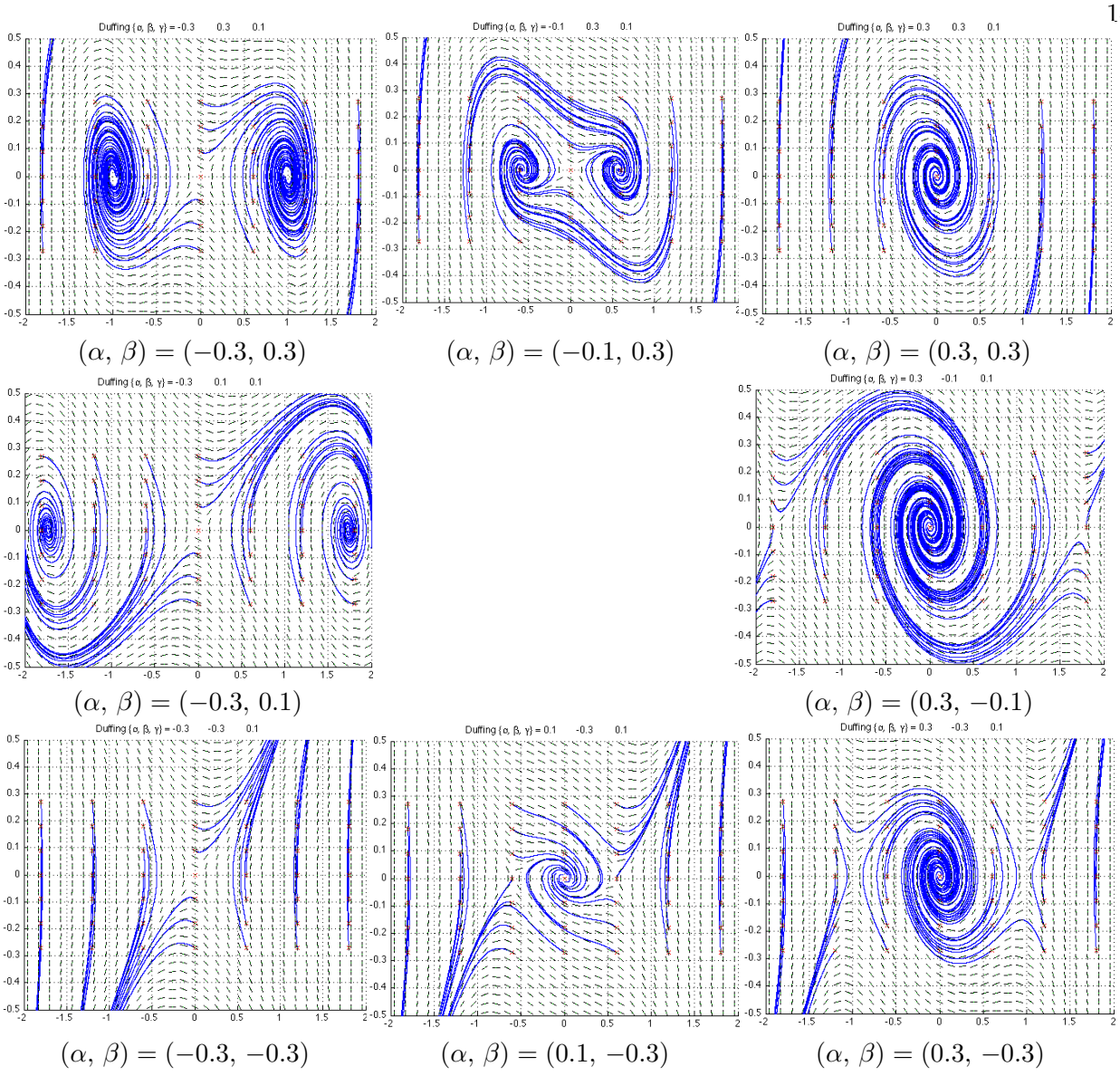

$(\alpha,\ \beta) = (-0.3,\ 0.3)$ $(\alpha,\ \beta) = (-0.1,\ 0.3)$ $(\alpha,\ \beta) = (0.3,\ 0.3)$

$(\alpha,\ \beta) = (-0.3,\ 0.1)$ $(\alpha,\ \beta) = (0.3,\ -0.1)$

$(\alpha,\ \beta) = (-0.3,\ -0.3)$ $(\alpha,\ \beta) = (0.1,\ -0.3)$ $(\alpha,\ \beta) = (0.3,\ -0.3)$

Figure 2.3: Duffing Phase Plane Plots, $\gamma = 0.1$

2.4.1 The Poincaré Map

Figure 2.4a shows the forward flow of the Duffing equation on the $(\dot{x}, x)$ phase-plane when driven by a periodic forcing function. In this case, $(\alpha, \beta, \gamma) = (0.3, 0.3, 0)$, $u(t) = 0.08\sin(2\pi 0.1087t)$, the initial condition is $(0, 0)$, and we have temporally varied the color from blue to green, yellow, orange, and finally red. Notice that we have overlapping trajectories because we have neglected to provide an ordinate for the time dependence of the input. A less ambiguous representation would

be to let $\theta = \omega t + \phi$ be a state on $\mathbb{S}^1$, rewriting our equations in autonomous form. However, the resulting three dimensional trajectory would be difficult to view. Enter Poincaré in 1890[4], who envisioned projecting the intersection of the flow on $\mathbb{R}^2$ cross-sections of $\mathbb{S}^1$ that align with the input frequency. The black points in Figure 2.4a are the initial Poincaré samples that eventually form the closed black curve in Figure 2.4b, called a first recurrence map, or Poincaré map. At a different toroidal cross section of the $\mathbb{S}^1 \times \mathbb{R}^2$ trajectory, the Poincaré map will likely change, but we can bound the extremities of all cross sections of the toroidal trajectory by including the ambiguous $(\dot{x}, x)$ trajectory in the background, here in orange. As we will see, the full trajectory sometimes highlights more complex inner workings when included with the Poincaré map.

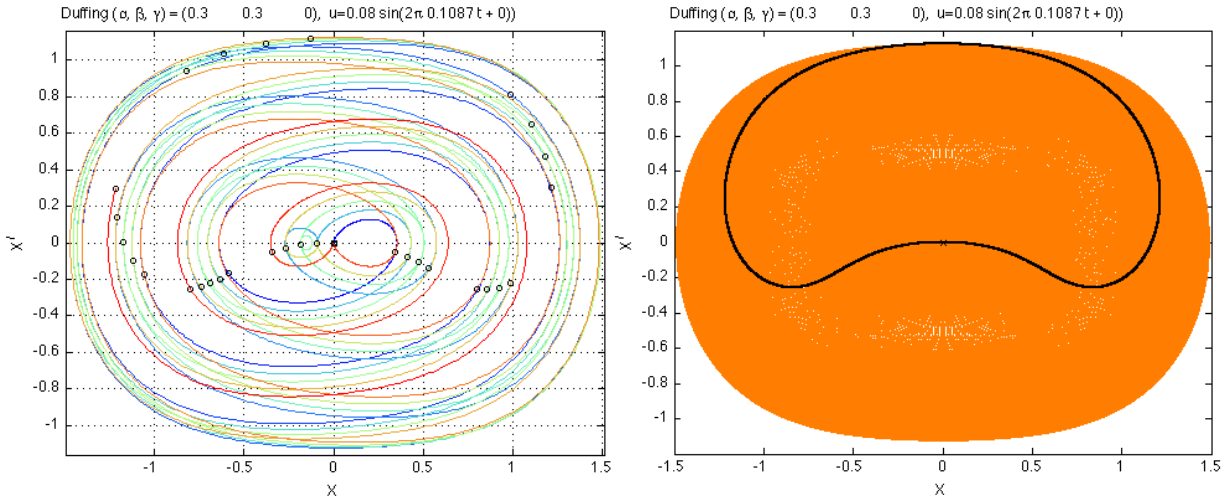

a) Temporally Colored Trajectory & Poincaré Samples (o)

b) Poincaré Map (black), Trajectory (orange)

Figure 2.4: Introducing the Poincaré Map

The Poincaré map offers quick insight toward characterizing system dynamics as either periodic, quasi-periodic, or chaotic. If a trajectory is periodic the Poincaré section will be crossed at the same point every time once transients have died out. Consider a damped spring model, which weakens at high displacement, being driven by a periodic forcing function. The color-coded phase plot and Poincaré sampling are shown in Figure 2.5, with initial condition $(0, 0)$, and other

parameters shown in the plot.

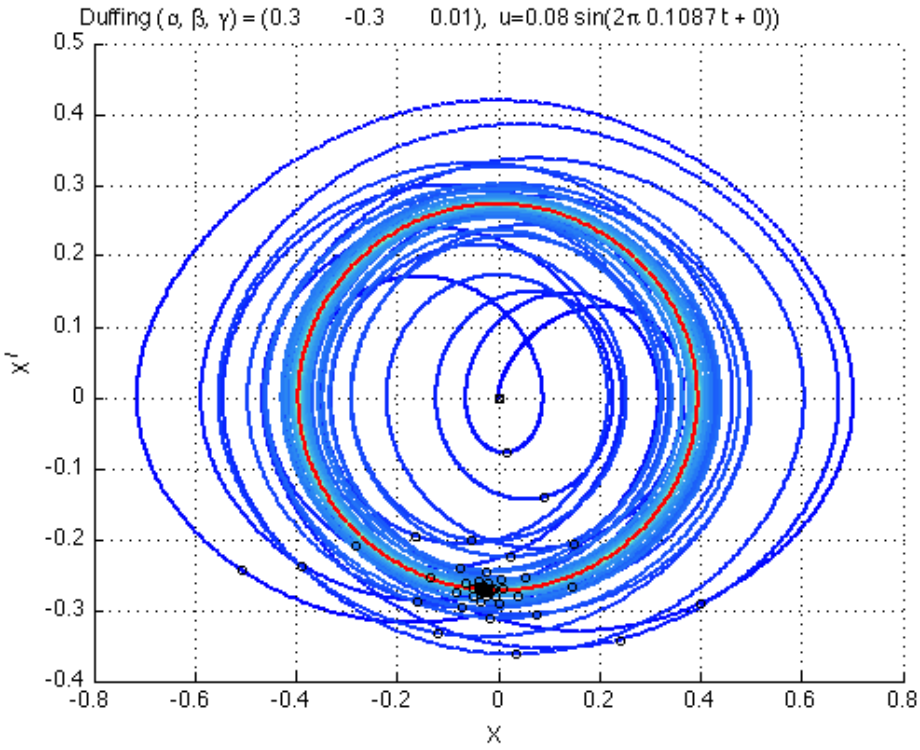

Poincaré Map in Black

Figure 2.5: Periodic Limit Cycle

Again, the trajectory starts out blue, then transitions to green, yellow, orange, and finally red. Figure 2.5 clearly shows the limit cycle in red. Notice that as the transient dynamics are dying away, the Poincaré map begins to converge to a single point, indicating the steady state dynamics are periodic.

When the Fourier spectra are discrete in nature, the Poincaré maps will be closed contours indicating that the solutions are quasi-periodic. Quasi-periodic dynamics have two or more discrete spectral components. Finally, chaotic trajectories have continuous spectral components and distributed Poincaré maps. The quasi-periodic and chaotic Poincaré maps are demonstrated in the next section.

2.4.2 The Onset of Chaos

Referring back to the upper-left Duffing parameterization shown in Figure 2.2, with $(\alpha, \beta, \gamma) = (-0.3, 0.3, 0)$, recall that this un-driven, undamped, Duffing model will oscillate given non-equilibrium initial conditions. In Figure 2.6 we show the effect of slowly increasing the amplitude of a periodic forcing function with non-commensurate frequency on the Poncaré disc. In each case the initial condition is $(x, \dot{x}) = (0.5, 0.1)$. As might be expected, at first we get a quasi-periodic solution which is the spectral superposition of the natural oscillatory frequency and the injected frequency. In the upper-left corner of Figure 2.6, note the clean closed contour of the Poincaré map with input $u = 0.004 \sin(\omega_i t)$. However, with a small increase in amplitude to 0.0043, the Poincaré map displays two loops and the clean closed contour becomes a narrow distribution of points. Further increases in amplitude continue to broaden and transform the "chaotic" Poincaré distribution.

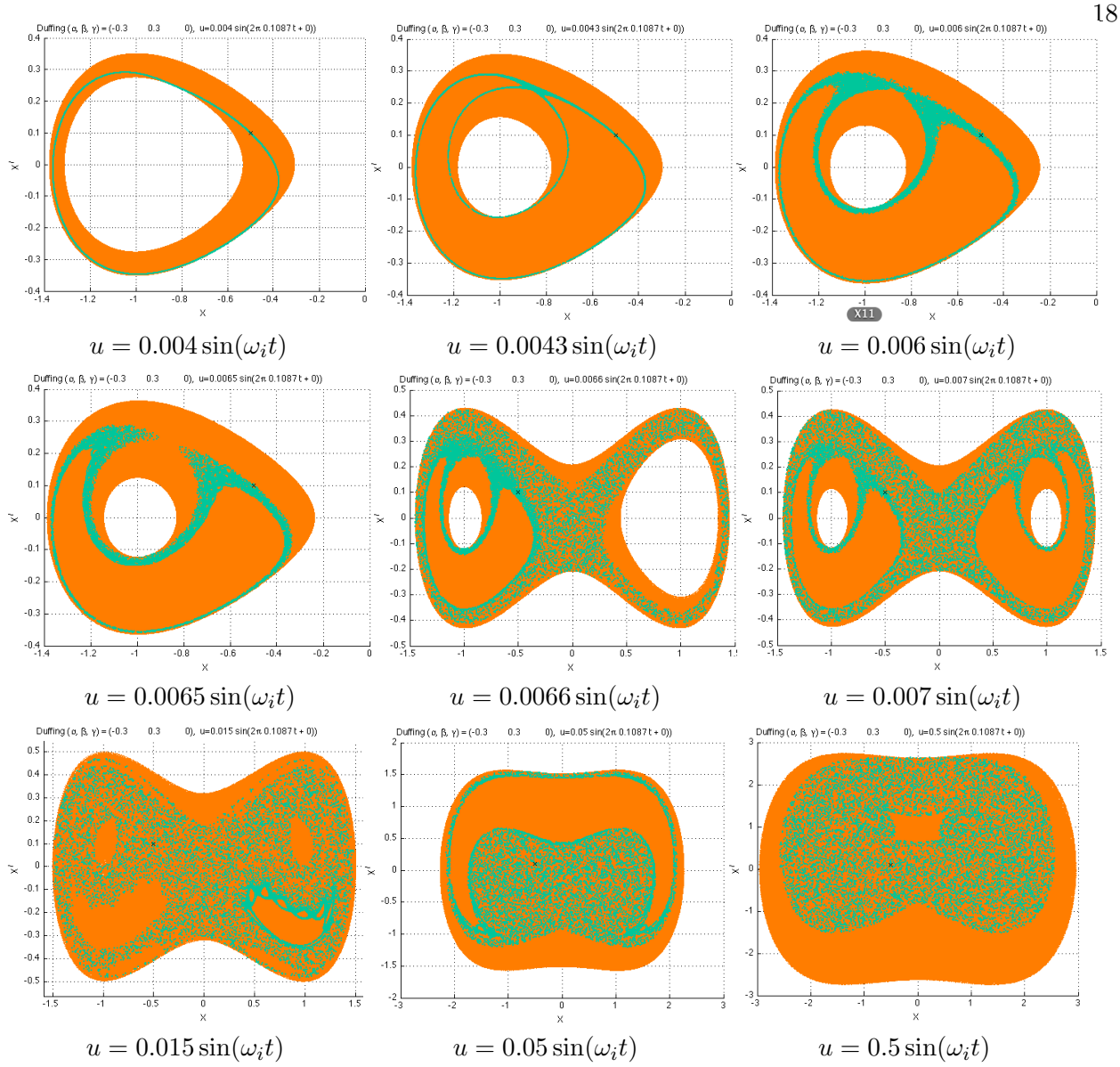

Figure 2.6: Poincaré Maps of Forced Duffing Eqn

2.4.3 Testing for Chaos

Erratic trajectories, non-closing Poincaré maps, and distributed power spectrums are all indicators of chaotic dynamics, especially when there exist only negligible sources of noise. There are more rigorous tests for chaos, the most common is computing Lyapunov exponents. However,

here we will explore the recently published "0-1 test for chaos."

The idea behind the 0-1 test is to determine if the dynamics are diffusive, thereby establishing a measure of unpredictability distinct from a noise process. Suppose we have a time series $\phi(j)$ that may or may not be chaotic. The 0-1 test can be applied directly to the data, noise and all. It is a statistical correlation with a limit of 1 for chaotic processes, and 0 for normal dynamics. There is no need for phase space reconstruction, no limitation on the dimensionality or type of vector field, nor a need to characterize inherent noise sources. With these advantages in mind, we warn the potential user that Romero-Bastida, Olivares-Robles, and Braun[5] recently found some erroneous and computationally untractable results for certain Hamiltonian systems.

Implementation of 0-1 Test[6]:

(1) Choose a sample time

In the limit as the number of samples goes to infinity, the results of the 0-1 Test are the same, independent of the sampling time. However, in practice, a poorly chosen sample time will bring the computation to a grinding halt. As published by Romero-Bastida, etc[5], the 0-1 test can be computationally intensive for some systems even when oversampling is addressed.

The most straightforward way to avoid oversampling is to choose the sample times, t_j, that correspond with intersections of the trajectory with a cross-section of the phase-plane, e.g. Poincaré samples. This is the approach taken throughout these investigations.

(2) Translation variables

For N observations of $\phi(\cdot)$, the translation variables are computed in quadrature in a way reminiscent of Fourier coefficients

$$p_c(n) = \sum_{j=1}^{n} \phi(j) \cos jc, \quad q_c(n) = \sum_{j=1}^{n} \phi(j) \sin jc$$

Where $n \in [1, N]$ and $c \in (\pi/5, 4\pi/5)$. These are the detectors of diffusive behavior foundational to the 0-1 test. Note that in contrast to Fourier coefficients, the translation

variables are computed over successively longer sums, providing temporal correlation with elliptical dynamics. How big N needs to be my require some debate.

For some discrete values of c, the translation variables cannot distinguish between diffusive and non-diffusive dynamics. Specifically, when the Fourier decomposition of the observation has a term proportional to $\exp(-i\omega k)$, there is a resonance detected in $p_c(n)$ at $c = \omega$, whether the dynamics are chaotic or not. For this reason, the 0-1 test is statistical in nature, whereby the angular frequency variable c, is uniformly sampled on $(0, \pi)$. Because significant sampling window artifacts occur near the boundaries, it is recommended to further restrict c to $(\pi/5, 4\pi/5)$.

(3) Mean square displacement of translation variables

We want to determine if there is linear, temporal growth of the variance in translation variables. The mean square displacement is use to measure this temporal growth as a function of n. Fixing c, it is defined as

$$M_c(n) = \lim_{N\to\infty} \frac{1}{N} \sum_{j=1}^{N} [p_c(j+n) - p_c(j)]^2 + [q_c(j+n) - q_c(j)]^2$$

Similar to an Allan variance, $M_c(2)$ is measuring the correlation at half the frequency as $M_c(1)$, and so forth.

(4) Linear correlation of mean square displacement.

Finally, to measure the linearity of the temporal growth we use the familiar correlation coefficient. Fixing c again, let $\xi = 1, 2, \ldots, n_{cut}$ and $\Delta = M_c(1), M_c(2), \ldots, M_c(n_{cut})$. Then

$$K_c = \frac{cov(\xi, \Delta)}{\sqrt{var(\xi) var(\Delta)}}$$

where

$$cov(x, y) = \frac{1}{m} \sum_{j=1}^{m} (x(j) - \bar{x})(y(j) - \bar{y}), \quad \bar{x} = \frac{1}{m} \sum_{j=1}^{m} x(j)$$

and

$$var(x) = cov(x, x)$$

If there is linear correlation in the $M_c(1,\ldots,n_{cut})$ sequence, for a given c, then $K_c = 1$, indicating diffusive, chaotic behavior. Otherwise, $K_c = 0$, indicates regular dynamics. Gottwald[6] suggests that statistical correlation of K_c is assured by calculating $M_c(n)$ for $n \geq N/10 \equiv n_{cut}$; and, this advice was followed in our study. To conclude the 0-1 test, we take the median value of K_c, over all randomly chosen values of $c \in (\pi/5, 4\pi/5)$, to remove outliers.

An interesting place to apply the 0-1 Test is at the transition from the quasi-periodic to chaotic dynamics, such as the one found in the first two Poincaré maps of Figure 2.6. Figure 2.7 and 2.8 show the distribution of K_c for an input amplitude of 0.004, and 0.0043 respectively. The resulting median K_c for these cases was $K = 0.0062$, and $K = 0.9965$, indicating no ambiguity in the 0-1 test for this narrow band chaos. Figure 2.9 shows an interesting test of the $K = 0.0062$ case using only half the samples. Although the Poincaré map has yet to elicit the full dynamics, we still achieve a positive 0-1 chaos test with $K = 0.9882$. In all of these cases, the initial condition remained $(x, \dot{x}) = (0.5, 0.1)$.

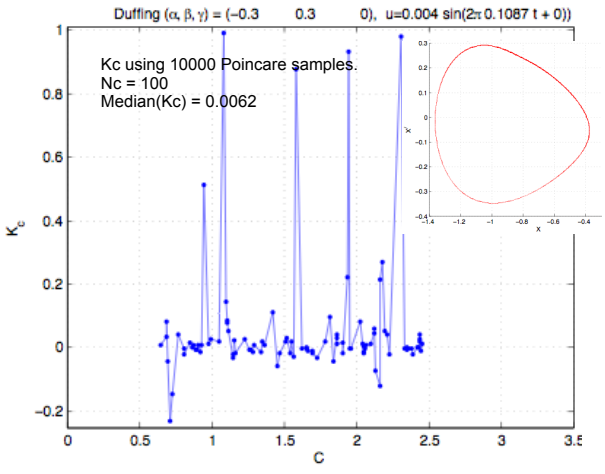

Figure 2.7: Zero-One Test, Quasi-periodic Result

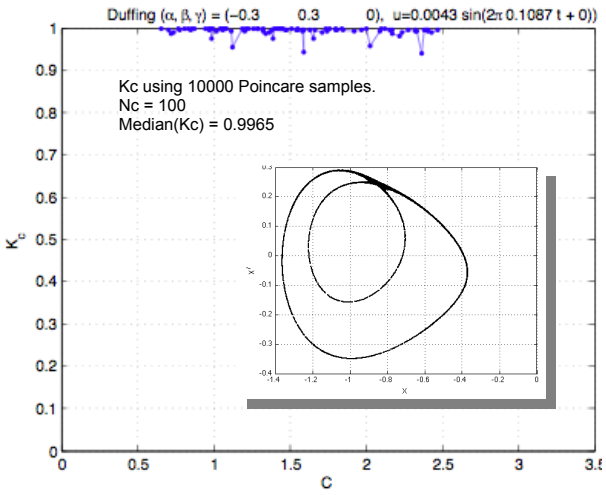

Figure 2.8: Zero-One Test, Chaotic Result

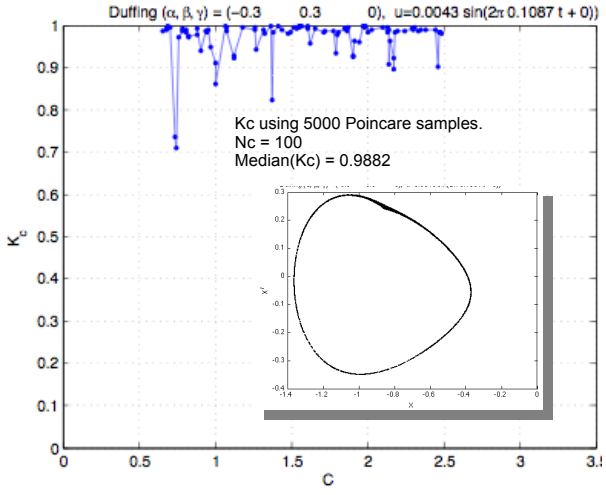

Figure 2.9: Zero-One Test, Short Sequence

2.5 Information at the Edge of Chaos

One surprising finding was that a chaotic trajectory was informative of the existence and boundaries of quasi-periodic trajectories. We demonstrate with a parameterization of the Duffing model. Duffing chaos has a well defined region constraining its unpredictability. Beyond the borders of this chaotic region are quasi-periodic orbits with closed Poincaré contours. Thus a single chaotic trajectory can be used to shed light on the existence of many quasi-periodic orbits.

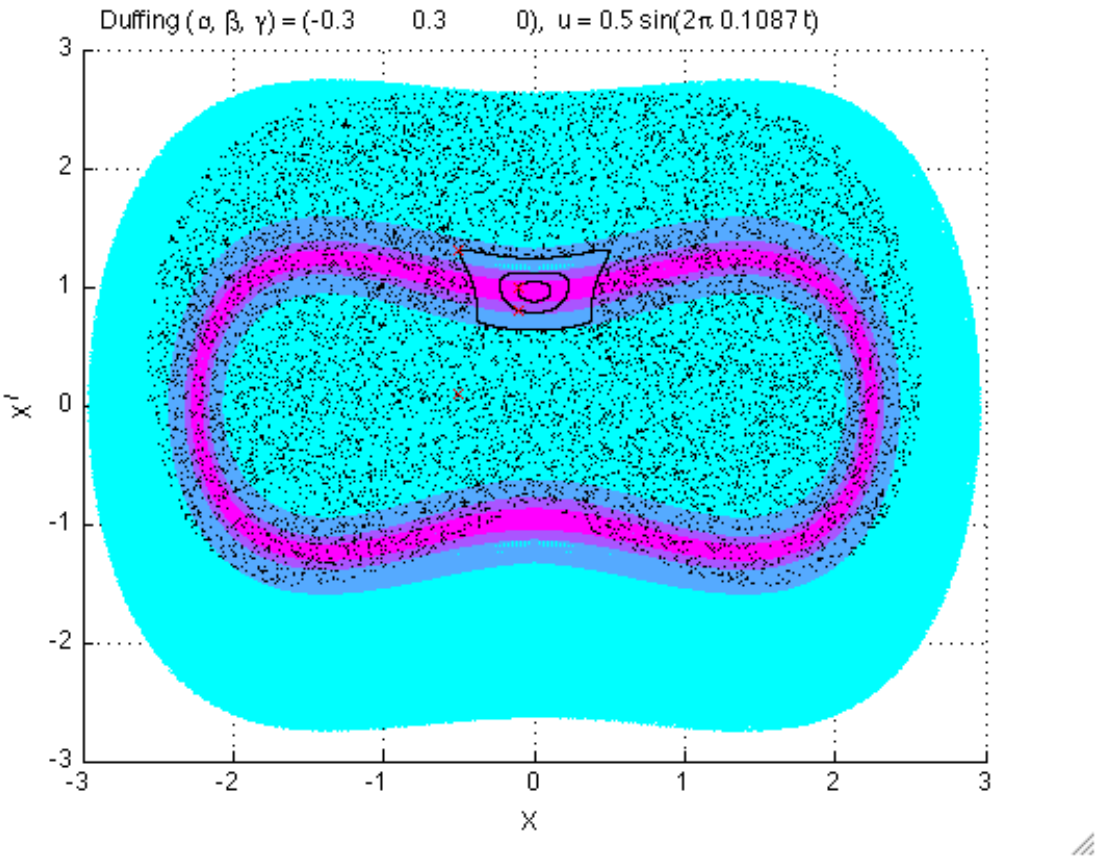

$\omega_i = 0.6823\, rad/s$, $(\alpha, \beta, \gamma) = (-0.3, 0.3, 0)$, $u = 0.5\sin(\omega_i t)$

Figure 2.10: Quasiperiodic Info at Chaotic Boundaries

Consider the forced Duffing parameterization given by the lower-right corner of Figure 2.6, with $u = 0.5\sin(\omega_i t)$, and initial condition $(-0.5, 0)$. We repeat this Poincaré map in Figure 2.10. Also shown in the figure (in black) are the Poincaré maps of the same system, but with initial

conditions of $(-0.5, 1.3)$; $(-0.1, 0.8)$; and $(-0.1, 1)$. Shown in four light colors are the regions which these Poincaré maps ride during their full trajectory; they form what looks like a Zorro mask. Finally, the initial conditions are displayed as red crosses. Notice there are three quasi-periodic orbits plotted across the forehead (of Zorro's mask) and a chaotic trajectory creating a cloud around the eyes, upper forehead, and over the nose.

The chaotic trajectory has an outer and inner border; note the non-chaotic region between the brows. When initial conditions are chosen beyond these borders, the Poincaré map forms closed contours as seen by the three closed contours found between the brows in Figure 2.10 and the contour show in Figure 2.11b. By zooming in on the brow, Figure 2.11a, we see that the closed Poincaré maps are subsets of intricate phase plane plots.

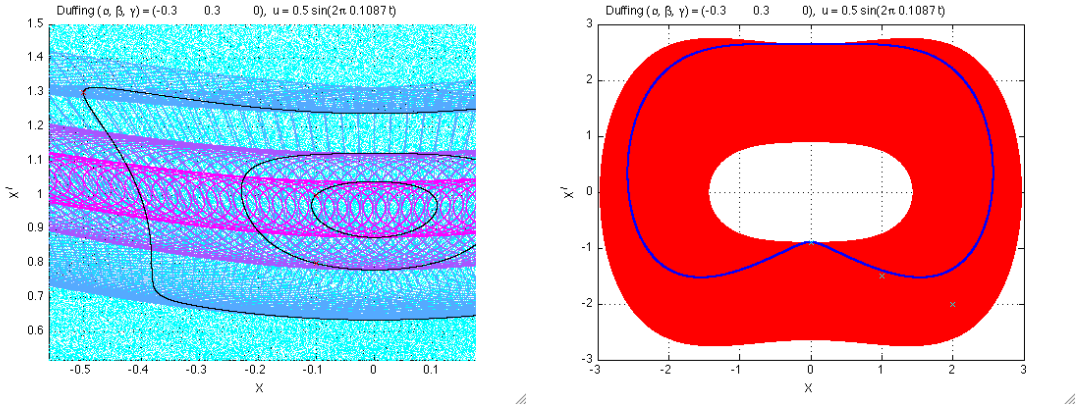

a) Inner Orbits b) Outer Orbits

Figure 2.11: Quasiperiodic Info at Chaotic Boundaries

So how are these observations useful? By visualizing one chaotic trajectory we gain insight into numerous sets of quasi-periodic modes that we would not otherwise predict. In this example, we have deduced that the chaotic trajectory has an invariant region, "chaotic invariant space," distinct from the quasi-periodic invariant space. Thus for initial conditions within the chaotic invariant space, we get a chaotic trajectory. Likewise for the quasi-periodic invariant space. It would be interesting to explore other systems and eventually attempt to determine if this is true for all lossless chaotic systems.

A more complex example can be shown from the chaotic trajectory in the lower-left corner of Figure 2.6, with $u = 0.015\sin(\omega t)$. In this case there is a complex set of non-intersected areas that prove to be quasi-periodic boundaries. In Figure 2.12, we explore some of these quasi-periodic trajectories at the boundaries of a chaotic trajectory. The distribution of green points is a Poincaré map of a chaotic orbit. The narrow lines are Poincaré maps of quasi-periodic orbits, each with a distinct color. Each orbit marks its initial condition with a black "x". The yellow orbit has eight distinct Poincaré islands. Notice that any open region adjacent to the chaotic trajectory can reliably predict the initial condition and conforming shape of a quasi-periodic orbit.

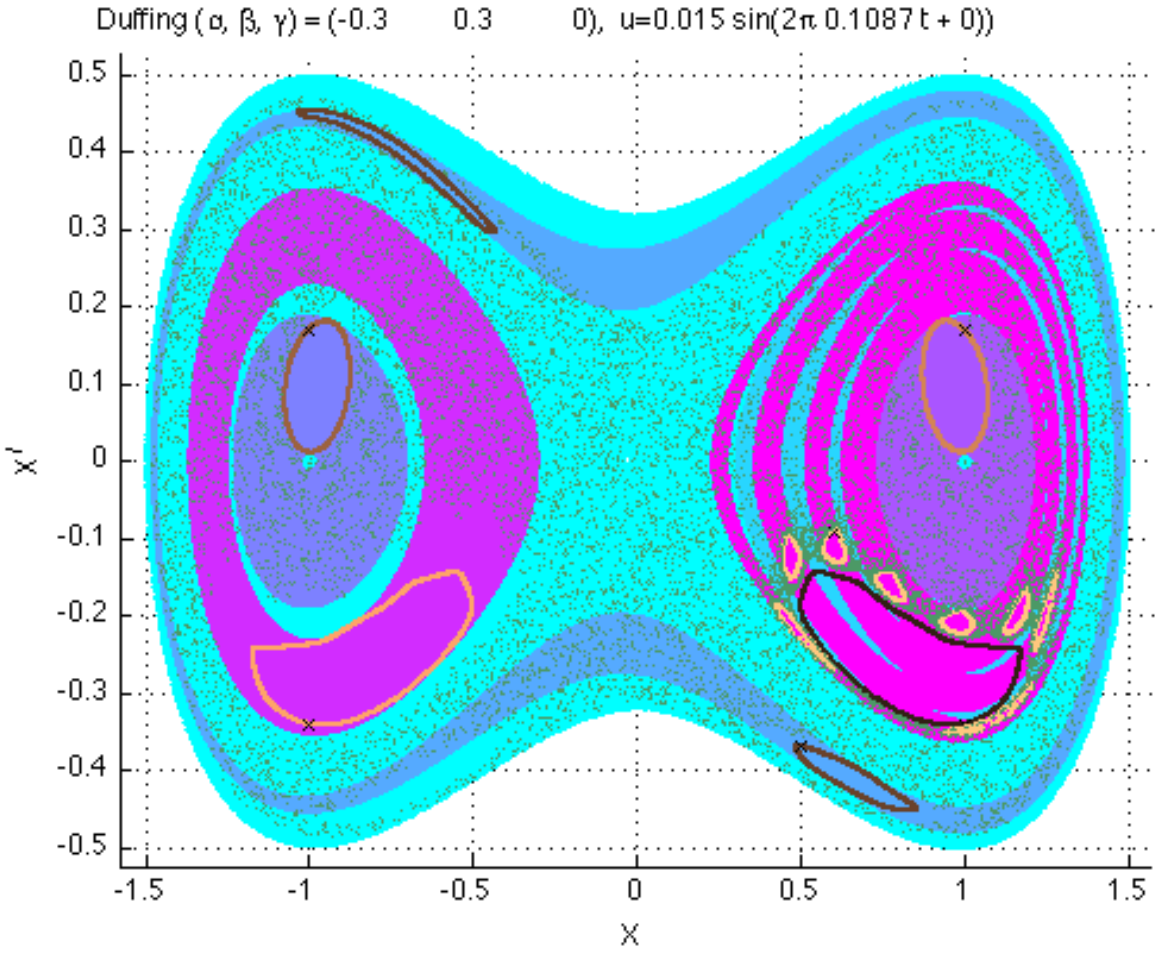

Figure 2.12: Quasiperiodic Info at Chaotic Boundaries

Chapter 3

The Van der Pol Oscillator

3.1 An Engineered Oscillator

In 1922, a Dutch electrical engineer by the name of Balthazar Van der Pol[7] studied active cancellation of dissipative effects occurring in a triode tube circuit. As a realization of Liénard's equation, the Van der Pol (VDP) oscillator complements the Duffing equation by placing the requisite nonlinearity into the damping term, $f_\delta(x)$, instead of the frequency term, $g_\omega(x)$. Moreover, it satisfies Liénard's theorem and is a practical model for an engineering frequency reference because it is a self-excited system with a parameter-fixed steady state frequency.

The Van der Pol oscillator is introduced because it is similar to many engineered oscillator designs and it has been extensively characterized by academia. Recall that the Liénard damping function, $f_\delta(x)$, tends to shape the signal, while the fundamental frequency is controlled by the restoring force function, $g_\omega(x)$. Engineered oscillators are typically similar to the Van der Pol oscillator in that the nonlinearity is found in $f_\delta(x)$, producing a saturating effect. The amplitude of these systems is relatively constant, being affected most by slowly varying parameters due to temperature fluctuations or environmental vibrations. It is also common for engineered oscillators to provide a small amount of frequency control with a biasing parameter in the restoring force function, $g_\omega(x, \beta)$. When the bias parameter is controlled by an external voltage, perhaps by means of a varactor, the result is a voltage controlled oscillator, which is discussed in Section 4.2.2 in the context of a phase-locked loop.

3.2 Van der Pol Model

In Figure 3.1, we consider compensating for the resistor losses in an LCR network with a parallel, voltage-dependent, current source. Let $i_n(v) = av + bv^3$ or equivalently, introduce an active, nonlinear conductance term $Q_n(v) = \frac{di(v)}{dv} = a + 3bv^2$.

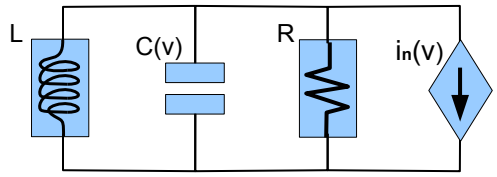

Figure 3.1: Van der Pol Circuit

The system equation becomes:

$$\frac{d^2v(t)}{dt^2} + \frac{1}{C}\left(Q_n(v(t)) + \frac{1}{R}\right)\frac{dv(t)}{dt} + \frac{1}{LC}v(t) = 0$$

$$\ddot{v} + \frac{1}{C}\left(Q_o + 3bv^2\right)\dot{v} + \frac{1}{LC}v = 0 \tag{3.1}$$

where $Q_o = a + 1/R$, is the total conductance (typically negative) when $v = 0$.

It is convenient to re-formulate in first-order form. With $x = v$, we have

$$\dot{x} = y - \frac{1}{C}x(Q_o + bx^2)$$
$$\dot{y} = -\frac{1}{LC}x$$

3.3 General Local/Global Dynamics of Van der Pol

First we take a look at how the local behavior is parameterized about the equilibrium point $(\dot{v}, v) = (0, 0)$. The characteristic eigenvalues of the linearization are obtained at

$$p_{1,2} = \frac{-Q_o}{2C} \pm \frac{\sqrt{(Q_o^2L^2 - 4LC}}{2LC}$$

To allow for a non-trivial steady state solution (and oscillator startup) we require that $Q_o < 0$, or equivalently, $a < -1/R$. This destabilizes the equilibrium point by providing a net negative conductance. So generally the equilibrium point is an unstable hyperbolic focus.

Next, we wish to verify that the Van der Pol oscillator has a unique, stable limit cycle. Because it has already been formulated to match Liénard's Theorem, with

$$g_\omega(x) = \frac{1}{LC}x, \quad F_\delta(x) = \frac{1}{C}x(Q_o + bx^2)$$

Conditions (i) through (v) of Liénard's Theorem are satisfied provided that $Q_o < 0$, and $b > 0$, which we will presume throughout.

Finally, from Section 1.5.4 we account for the energy dynamics

$$H(x,y) = \frac{1}{2}\left(y^2 + \frac{1}{LC}x^2\right)$$

$$\frac{dH}{dt} = -\frac{1}{LC^2}x^2\left(Q_o + bx^2\right)$$

This shows that the Van der Pol oscillator will increase oscillatory energy for $x^2 < -Q_o/b$ while providing Lyapunov stable dissipative effects for large values of $|x|$. This can be seen for a specific parameterization in Figure 3.2a in the section that follows.

3.4 Van der Pol Simulation

To demonstrate the VDP oscillator, we realize (3.1) with $L = 1nH$, $C = 10pF$, $Q_o = -0.02$ and $b = 0.01$. Figure 3.2b shows the associated limit cycle from two initial conditions, $(x(0), \dot{x}(0)) = \{(0.1,\, 0.1)\ \&\ (-2.5,\, 2 \cdot 10^{10})\}$. The simulated startup transient for the first IC is shown in Figure 3.2c. In the same figure we plot the behavior of the damping term, $\left(1/R + Q_n(v(t))\right)/C$, normalized to unity. The nonlinearity eventually causes the damping term to rise above zero each half cycle, constraining the exponential growth of the signal.

Near to equilibrium we know the voltage will be an exponentially growing sinusoid. The amplitude of the transient response begins to level out as the orbit enters the limit-cycle. Although it still visually appears sinusoidal, the power spectrum, shown in Figure 3.2d, indicates that it is beginning to take on odd-harmonics. This means that the signal's amplitude is being shaped by system parameters into a square wave. This is a common theme found in the design of autonomous oscillators and will be exploited by the phase-locked loop in Section 3.0.

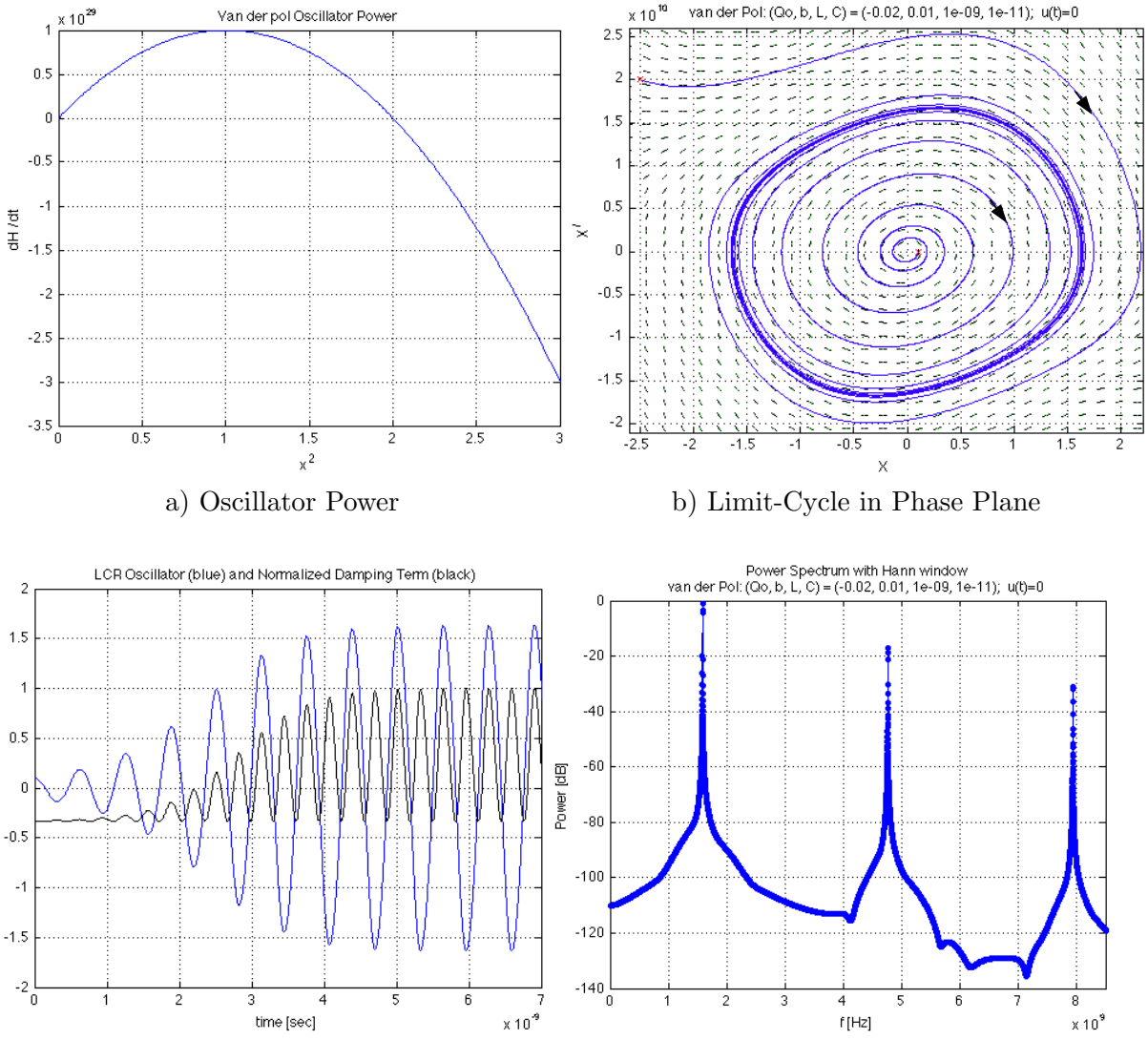

a) Oscillator Power

b) Limit-Cycle in Phase Plane

c) Startup Transient

d) Undriven Power Spectrum

Figure 3.2: Van der Pol Simulation Plots

The resulting nonlinear system has a steady state frequency of approximately 1.5876 GHz, and several odd harmonics, as shown in Figure 3.2d. Interestingly, this is the mean between the undamped and damped natural frequency of the system linearized about $v = 0$.

$$\omega_n = \sqrt{1/(LC)} \approx 2\pi \cdot 1.59155\, GHz$$

$$\omega_d = \sqrt{-Q_o^2 L^2 + 4LC}/(2LC) \approx 2\pi \cdot 1.58357\, GHz$$

3.5 Forced Van der Pol

To push the Van der Pol model further, we consider injecting a sinusoidal current $i_s(t) = A\cos(\omega_s t)$ in parallel to the original circuit. When ω_n/ω_s is not rational we obtain quasi-periodic solutions. The damping causes Poincaré maps from distinct initial conditions to converge for the driven Van der Pol oscillator. We show two partial Poincaré maps in black and gray in Figure 3.3 with the same initial conditions as the previous case.

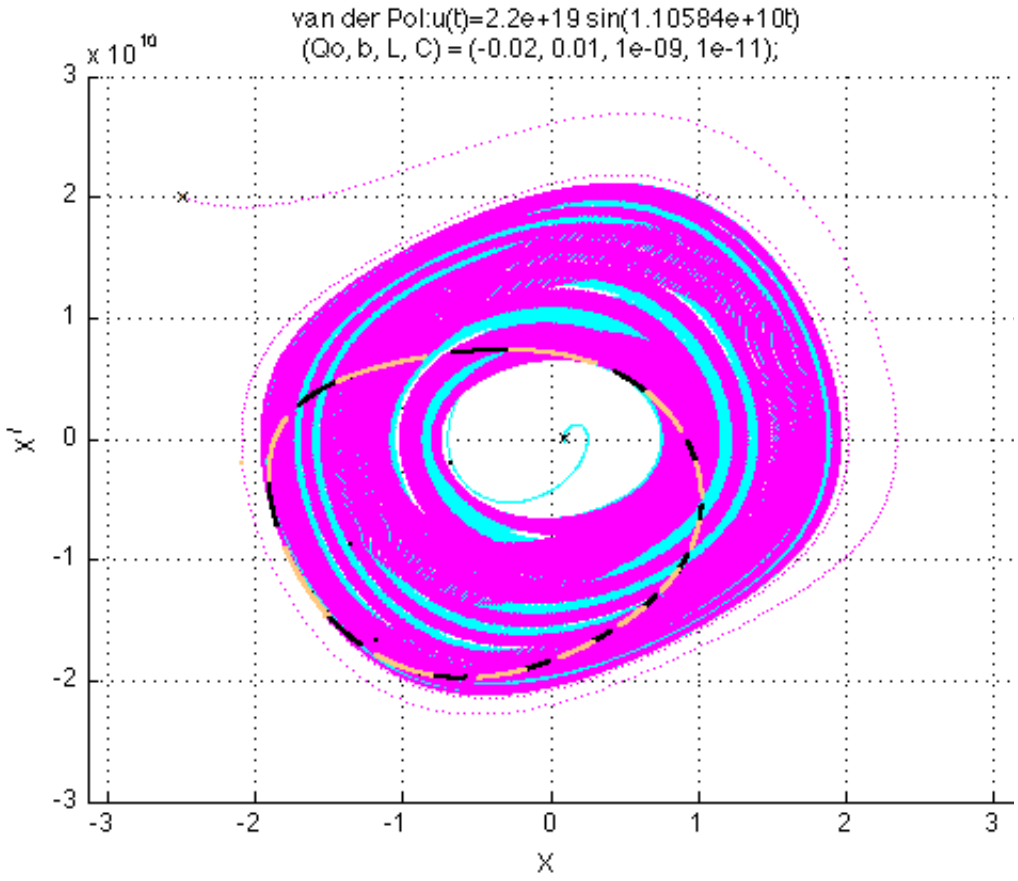

Figure 3.3: Forced Poincaré Map

We plot the transient response and power spectrum of this system with $(x(0), \dot{x}(0)) = (0.1, 0.1)$ in Figure 3.4. The steady-state driven response resembles an amplitude modulated sawtooth wave. The Hann sampled power spectrum demonstrates discrete spectra with fundamentals of 1.6133 GHz at -1.96 dB , and 1.76 GHz (the driving frequency) at -4.5 dB, along with many subharmonics with a comb pitch of 146.7 MHz.

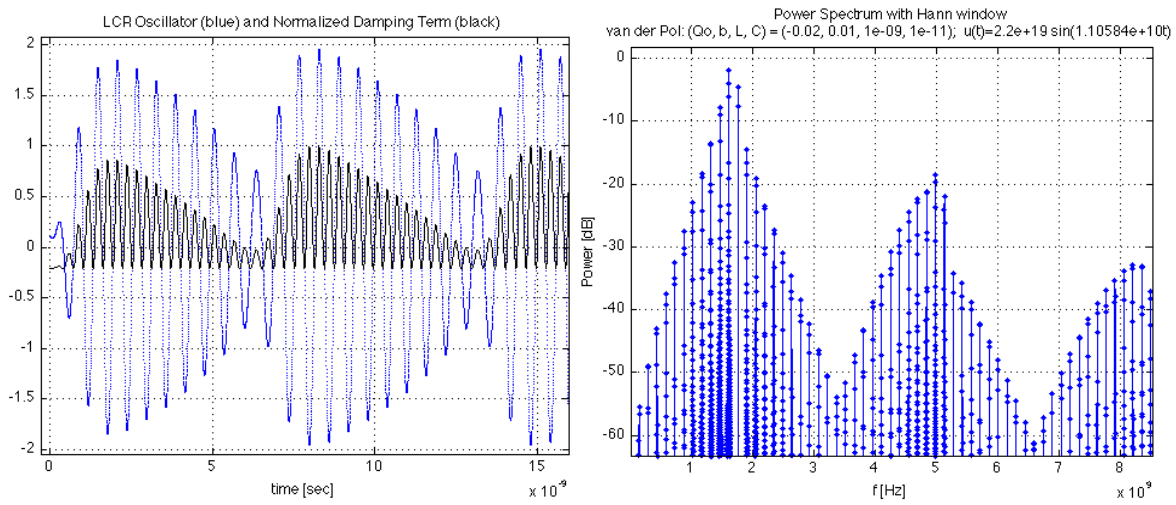

a) Transient VDP Response b) Driven VDP Spectrum

Figure 3.4: Forced Poincaré, Time and Frequency Analysis

A lot of academic interest has been put into the Van der Pol equation. It can be shown that it undergoes an Andronov-Hopf bifurcation as the resistance crosses zero.[2] Although it is capable of chaotic behavior, achieving appropriate initial conditions is nontrivial.[8][9]

Chapter 4

Synchronization and the Phase-Locked Loop

4.1 Synchronization

Synchronization describes the interaction of rhythmic systems resulting in correlated frequency or phase. This often occurs by means of a minimal energy process in which discrete physical systems attempt to coexist . In the 17^{th} century, the inventor of the pendulum clock, Christiaan Huygens, observed the synchronization of his clocks when mounted to the same beam[10]. The more you look, synchronization is everywhere. Independently oscillating cardiac cells synchronize with adjacent neighbors to coordinate a heart beat. Learning can be described as a synchronization process within a neural network. Moreover, an entire culture can be described as learning networks synchronized to locally influential stimuli. Many of the fundamental elements of life involve synchronization. The most fundamental tool to understand synchronization is the phase-locked loop (PLL). Interestingly, second-order PLLs conform with Liénard's equation.

4.2 The Topology of the Phase-Locked Loop

4.2.1 Phase Model

The phase-locked loop (PLL) is a nonlinear augmentation to an open-loop oscillator common to communications and engineering. Typically it is used as a control system designed to either filter out noise of a reference oscillator (narrow bandwidth design), or stabilize a high frequency oscillator to a more stable reference oscillator (wide bandwidth design). We incorporate material

from Gardner[11], and Best[12].

The phase model we introduce is valid under the assumption that the phase can be inferred from a signal. Essentially, this means that the amplitude is not a significant time dependent variable either because the signal is generated from an oscillator whose amplitude is saturated (like a limit-cycle oscillator), or the nonlinear phase detector (to be discussed) treats the signals as though they are saturated. Like the Van der Pol oscillator, most engineered oscillators are self-excited and provide saturating limits. The amplitudes are nonlinearly attenuated, shaping the output into a square-wave as in Section 3.4. The resulting amplitude of the signal is a function of system parameters, like temperature or external vibrations, which vary slowly compared to the oscillator frequency.

The PLL consists of a phase detector, a filter, and a voltage controlled oscillator (VCO). We can model the PLL in terms of the phase. The primary components and topology are shown in terms of the phase model in Figure 4.1. They will be discussed in turn.

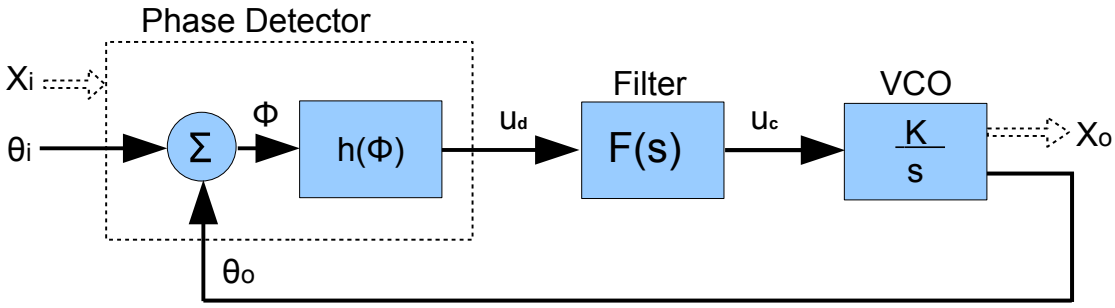

Figure 4.1: Phase Model of PLL

Here we presume that the reference input and PLL output, $X_i(t)$ and $X_o(t)$, are nearly periodic, differentiable signals. These signals provide input and output phase $\tilde{\theta}_i(t)$ and $\tilde{\theta}_o(t)$. To remove the ramped phase response of a periodic reference, we redefine the phases in terms of the unbiased angular frequency of the voltage controlled oscillator, ω_o. As a working example, the following sinusoidal signal definitions are useful in conjunction with an analog multiplier performing

quadrature phase detection.

$$X_i(t) = A\cos(\tilde{\theta}_i(t)), \quad \tilde{\theta}_i(t) = \theta_i(t) + \omega_o t$$

$$X_o(t) = B\sin(\tilde{\theta}_o(t)), \quad \tilde{\theta}_o(t) = \theta_o(t) + \omega_o t$$

4.2.2 Voltage Controlled Oscillator

To qualify as a PLL, the loop must have at least one integrator; otherwise, we have a regenerative divider topology[13]. This requirement is typically met by the voltage controlled oscillator (VCO). A VCO is an oscillator with a dynamic parameter used to control the oscillator's frequency. Recall from Liénard's oscillator equation, Eqn 3, that $g_\omega(x)$ determines the oscillator frequency. A bias converter, such as a varactor, translates the filtered phase error into a frequency dependent parameter offset $g_\omega(x, \epsilon)$, inducing a frequency change. As phase is the integral of frequency, the VCO can be modeled to first-order as a phase integrator with an unbiased angular frequency of ω_o,

$$\frac{d\tilde{\theta}_o(t)}{dt} = \omega_o + K_o u_c(t),$$

The VCO is typically not the same frequency as the reference. Usually a frequency divider or multiplier is incorporated after the VCO to align with the reference frequency. In Figure 4.1, we define our phases with respect to the phase detector inputs, hiding any internal frequency scaling within the loop.

There are many types of VCOs. Practical oscillators have tunable limits and other nonlinearities limiting the region over which the PLL can lock. Rather than exploring nonlinear VCO effects, we will focus on the nonlinearities in the phase detector.

4.2.3 Phase Detector

The phase detector is the heart of the phase-locked loop and the phenomena of synchronization. The purpose of the phase detector is to compare the phase of the VCO with that of the

reference. We define the phase error in our model as

$$\phi = \theta_i - \theta_o \in (\mathbb{S}^1 \mod 2\pi)$$

and denote phase detector's action on the phase error by $h(\phi)$.

There are several forms of phase detectors in use. For the purpose of this paper, we will restrict our interest to the analog multiplier, $u_d = X_i X_o$. Notice for ideal multiplication of two quadrature sinusoids we have

$$\begin{aligned} u_d &= X_i \cdot X_o \\ &= A\sin(\omega_i t) \cdot B\cos(\omega_o t - \phi(t)) \\ &= AB/2\left[\sin\left((\omega_i - \omega_o)t + \phi(t)\right) + \left(\sin\left((\omega_i + \omega_o)t + \phi(t)\right)\right]\right. \end{aligned}$$

Commonly, the high frequency component, $\omega_i + \omega_o$, is strongly attenuated by the filter and can be neglect in the phase detector's description. Without loss of generality we let $\omega_o = \omega_i$ and account for frequency/phase differences in $\phi(t)$. The multiplier's output is thus proportional to $\sin\phi(t)$.

$$u_d = h(\phi(t)) = K_d \sin\phi(t)$$

Given a phase-locked condition with $|\phi(t)| << 1$, the analog multiplier approximates linear phase detection, $h(\phi(t)) \approx K_d\,\phi(t)$ with periodic ambiguity. This is typical of most kinds of phase detectors. The slope K_d, defines the sensitivity of the phase detector. For our purposes, it is convenient to let $h'(0) = 1$, and incorporate the phase detector's sensitivity in the total loop gain, K.

In case this example seems like a contrived, anecdotal system, note that any nonlinear phenomena results in multiplication, as can easily be seen from a Taylor expansion in one or more variables.

Suppose for instance that $f(\cdot)$ is a nonlinear functional in a Hilbert space normally operating about some real valued function x_o. Let $z = y_1 + y_2$ be an additive disturbance to f about x_o.

Then the Taylor expansion in one variable is

$$f(x_o + z) = f(x_o) + D_x f(x_o) \circ z + \frac{1}{2} D_x^2 f(x_o) \circ z^2 + o(\|(z)^2\|)$$

where D_x denotes Frechét differentiation. The term $z^2 = y_1^2 + 2y_1y_2 + y_2^2$ introduces analog multiplication of the terms composing z. This mechanism, as well as others, phase-detectors arise from the inherent nonlinearities of a system.

4.2.4 The Loop "Filter", $F(s)$

The last component of the PLL, the filter, is somewhat of a wild card as it is tailored to meet criteria of each application. In engineering applications, active filters/controllers are designed to achieve performance goals of the system linearized about phase-lock. With these in mind, we represent the filter with Laplace transform notation, $F(s)$. However, many researchers have explored nonlinear characteristics in PLLs requiring more specific representation than shown in Figure 4.1. One might allow for additional nonlinear blocks on both sides of the VCO to incorporate additional model details. But first, we explore common linear filters, which are often applicable for small-signal analysis about the lock condition.

Linear PLLs can be characterized by the order of the system and the number of loop integrators, known as the type. The most common PLL designs in engineering are third-order, type II. Second-order type I and type II occur frequently in nature and make an interesting study. In Section 5 we explore the dynamic equations that result from a specific realization of the PLL using a lead-lag filter. The resulting system is equation (16). Before focusing on any specific nonlinear realization, we show how synchronization works near the phase-lock condition using linearization about equilibria of general second-order PLLs.

4.3 Linear Analysis of Phase-Locked Oscillators

4.3.1 Synchronization and Phase Noise

Before including nonlinear complications, it is important to understand synchronization of oscillators from a simple linear perspective. We can use phase-noise analysis to aid our understanding of the synchronization phenomena. Roughly speaking, phase-noise is a statistical measure of the variation in phase between two periodic processes. Rubiola[14] provides a nice reference on phase-noise. Two free-running oscillators will have uncorrelated phase-noise processes. When a VCO is phase-locked with a reference, its phase-noise is compared with the reference by the phase comparator. The VCO's phase error with respect to the reference is converted to a voltage and rejected by means of the compensator. The result is that within the bandwidth of the PLL, the VCO beats to the drum of the reference oscillator.

4.3.2 Example: Phase-Locked Oscillator

We consider a linear analysis of the phase-noise in a second-order PLL. Consider phase-noise being injected into the phase model as in Figure 4.2.

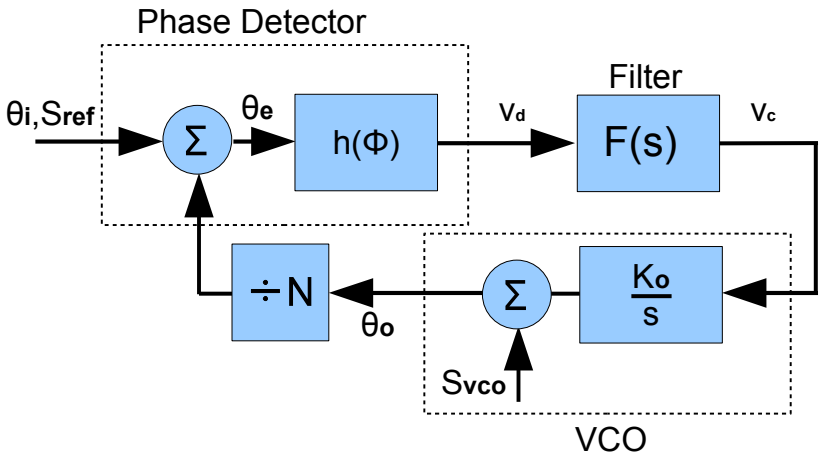

Figure 4.2: Phase-noise From Phase-locked Oscillators

Denote the phase noise two-sided power spectrum (noise spectrum) of the reference by S_{ref}, and that of the free-running VCO by S_{vco}. Further denote the transfer function from θ_i to θ_o by $H(\omega)$, and the transfer function from θ_i to θ_e by $E(\omega)$. Then we have the following relationships between the noise spectra:

$$\frac{\theta_o(\omega)}{\theta_i(\omega)} = H(\omega), \quad E(\omega) = 1 - H(\omega)$$

$$S_o(\omega) = |H(\omega)|^2 \cdot S_{ref}, \quad S_o(\omega) = |E(\omega)|^2 \cdot S_{vco}$$

A quality 5 MHz quartz oscillator will typically achieve -120 dBc/Hz at 1 Hz offset. When ideally multiplied up to 100 MHz, this equates to -94 dBc/Hz. Compare this with the -70 dBc/Hz at 1 Hz offset typically achievable with a free-running 100 MHz oscillator. However, the thermal noise of the 5 MHz oscillator, around -175 dBc/Hz shows up at offsets above 1 kHz. When this is ideally multiplied up to 100 MHz, we end up with a -149 dBc/Hz, significantly deteriorating our white noise floor where a free-running 100 MHz oscillator remains at -175 dBc/Hz. By phase-locking, we hope to achieve the best performance of both oscillators. The frequency at which the ideally multiplied phase noise of the reference intersects the VCO phase noise is called the crossover point.

Recall that $F(s)$ is a designed filter/compensator. Perhaps the most fundamental design goal for this example is to achieve a phase-lock with a bandwidth near to the crossover point. Because the phase error is negligible under the phase-lock condition, we can use linear analysis to design the filter such that the transfer function, $H(\omega)$ suits our needs. For simplicity, presume we designed $F(s)$ such that $H(\omega)$ is a standard second-order linear system with band-width ω_n. The magnitude response of $H(\omega)$ and $E(\omega)$ is shown in Figure 4.3 for $\omega_n = 2\pi \cdot 400$, and $\zeta = 1/\sqrt{2}$.

$$H(\omega) = \frac{2\zeta\omega_n s + \omega_n^2}{s^2 + 2\zeta\omega_n s + \omega_n^2}$$

We solidify our example with phase noise specifications from quality quartz oscillators available from industry. Figure 4.4 shows discrete phase noise specifications from a 5 MHz and 100

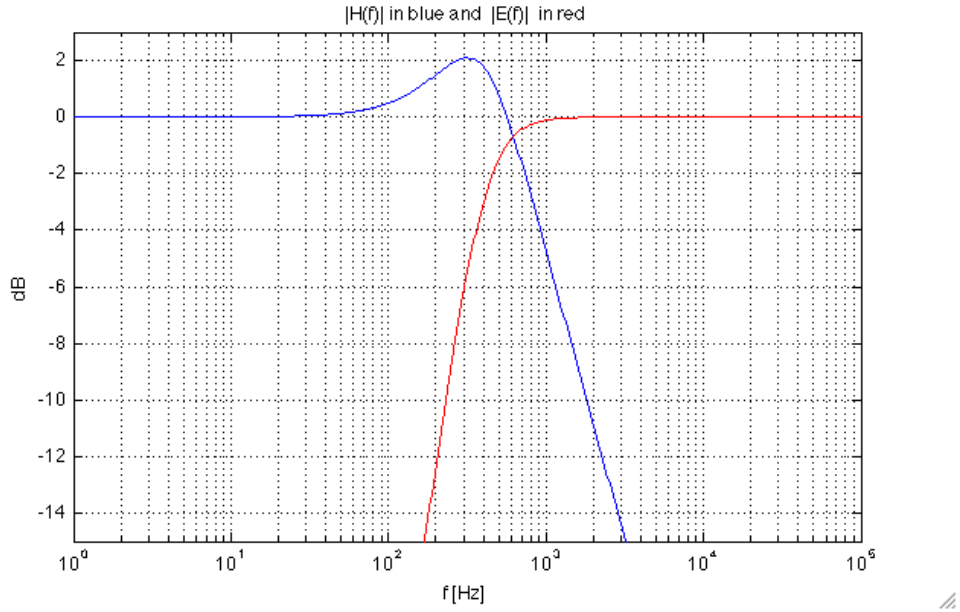

Magnitude Response with $\omega_n = 2\pi \cdot 400$, $\zeta = 1/\sqrt{2}$

Figure 4.3: Example Second-order Design

MHz quartz oscillator available from Wenzel Associates, Inc. The dashed lines are logarithmically interpolated equivalent noises when scaled to 100 MHz. Finally, the solid line shows the phase noise of the phase-locked 100 MHz oscillator. Although it has by no means been optimized, we have improved our phase noise by 25 dBc/Hz at low and high frequencies at the cost of only about 2 dBc/Hz phase-noise degredation around the crossover frequency (400 Hz.) Practical implementations would use at least a third-order, type II PLL, with linear quadratic optimization over the phase noise spectra of interest. This example has met our goal of using phase-noise to understand synchronization in the PLL. The VCO will beat to the drum of the reference within the bandwidth of the PLL, and beat to its own drum beyond that.

A phase-lock is defined as a proportionality between the phase variations of the VCO and the phase variations of the reference within the bandwidth of the loop. Much to-do is made over inherent limits on the control signal and the controllability of a VCO which define the locking bandwidth and subtle variations thereof. This type of analysis is specific for different types of

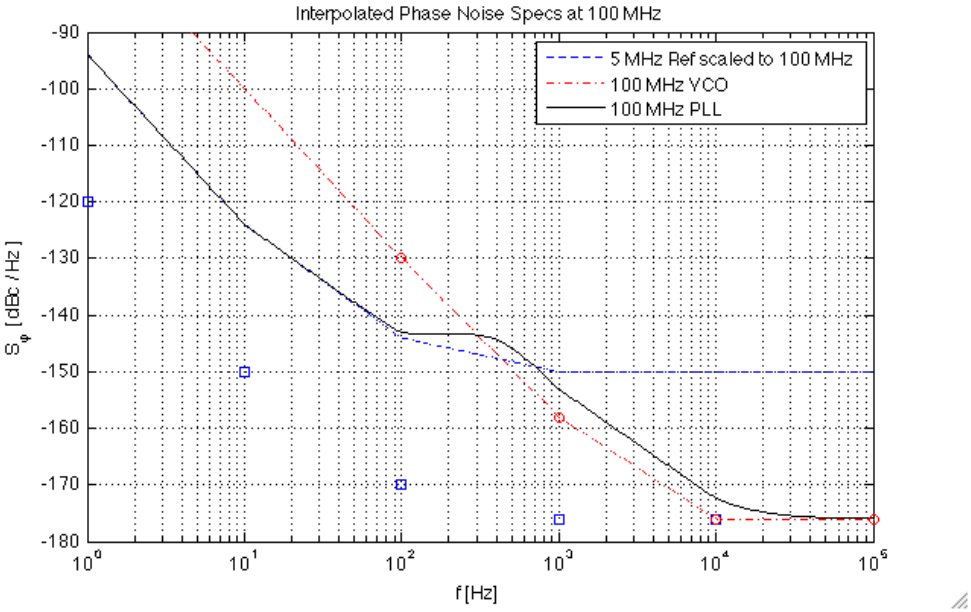

Figure 4.4: Resulting Phase Noise of Phase-Locked Oscillator

PLLs and may be found in numerous books; we will not focus on it.

4.4 Nonlinear Second-Order, Type I PLL

4.4.1 PLL Model Using a Lead-Lag Filter

A common implementation of a second-order PLL uses a lead-lag filter. The Laplace transform of this filter with unity gain is

$$F(s) = \frac{1 + \tau_1 s}{1 + \tau_2 s} \tag{4.1}$$

Using this filter and an analog multiplier for a phase detector, the PLL in Figure 4.1 can be modeled with two state variables, a pure integrator provided by the VCO and the filter pole at $1/\tau_2$. Our differential equation becomes

$$\begin{aligned} u_c + \tau_1 \dot{u}_c &= u_d + \tau_2 \dot{u}_d \\ &= h(\phi) + \tau_2 h'(\phi)\dot{\phi} \end{aligned}$$

$$\begin{aligned} \ddot{\theta}_i - \ddot{\phi} &= \ddot{\theta}_o \\ &= K\dot{u}_c \\ &= \frac{K}{\tau_1}\left(h(\phi) + \tau_2 h'(\phi)\dot{\phi} - \frac{1}{K}(\dot{\theta}_i - \dot{\phi})\right) \end{aligned}$$

$$\ddot{\phi} + \left(\frac{1}{\tau_1} + \frac{K\tau_2}{\tau_1}h'(\phi)\right)\dot{\phi} + \frac{K}{\tau_1}h(\phi) = \ddot{\theta}_i + \frac{1}{\tau_1}\dot{\theta}_i \tag{4.2}$$

We recall from Liénard's oscillator model that $h(\phi)$ is positioned to control the frequency of the loop and the damping (shape) is a function of $h'(\phi)$. Notice that the first order simplification, $h(\phi) = \phi$, effectively linearizes (4.2).

We can parameterize our equation in terms of linear, second-order dynamics. Let the natural angular frequency (ω_n) and damping coefficient (ζ) be defined as

$$\omega_n \equiv \sqrt{K/\tau_1}, \quad \zeta \equiv \frac{1 + K\tau_2}{2\sqrt{K\tau_1}}$$

Then,

$$\ddot{\phi} + \left(\frac{1}{\tau_1} + \left[2\zeta\omega_n - \frac{1}{\tau_1}\right] h'(\phi)\right)\dot{\phi} + \omega_n^2 h(\phi) = \ddot{\theta}_i + \frac{1}{\tau_1}\dot{\theta}_i \tag{4.3}$$

To the degree that the approximation $h(\phi) \approx \phi \in (\mathbb{S}^1 \mod 2\pi)$ holds, we achieve the second-order harmonic oscillator(2) with equilibria $(\dot{\phi}, \phi) = (0, 2\pi n)$, where $n \in \mathbb{Z}$.

4.4.2 Sinusoidal Phase-modulated Input Analysis

We constrain the inputs under consideration to be phase modulated sinusoids,

$$\frac{d\tilde{\theta}_i(t)}{dt} = \omega_c + M\sin\omega_m t$$

so that the inputs can be written as

$$\ddot{\theta}_i + \frac{1}{\tau_1}\dot{\theta}_i = M\omega_m\cos(\omega_m t) + \frac{1}{\tau_1}\left(\Delta\omega + M\sin\omega_m t\right) \tag{4.4}$$

where $\Delta\omega = \omega_c - \omega_o$.

4.4.3 The Normalized PLL Model

Finally, to maintain consistency with existing literature[15] we include the following normalization procedure. Define:

$\beta \equiv \omega_n/K$	normalized natural frequency
$\sigma \equiv \Delta\omega/\omega_n$	normalized frequency detuning
$\Omega \equiv \omega_m/\omega_n$	normalized modulation frequency
$m \equiv M/\omega_n$	normalized maximum frequency deviation
$t \to t/\omega_n$	normalized time variable change

Applying the phase modulated inputs and these normalized parameters our equation becomes

$$\ddot{\phi} + \left(\beta + [2\zeta - \beta]\, h'(\phi)\right)\dot{\phi} + h(\phi) = \beta\sigma + \beta m\sin\Omega t + m\Omega\cos\Omega t \tag{4.5}$$

Using analog multiplication for quadrature phase detection, $h(\phi) = \sin\phi$, we finally obtain a concrete model, worthy of dynamic analysis.

$$\ddot{\phi} + (\beta + [2\zeta - \beta]\cos\phi)\,\dot{\phi} + \sin\phi = \beta\sigma + \beta m \sin\Omega t + m\Omega\cos\Omega t \tag{4.6}$$

With $x = \phi$, and $y = \dot{\phi}$, we can formulate the following first-order equivalent model.

$$\dot{x} = y$$

$$\dot{y} = -(\beta + [2\zeta - \beta]\cos(x))y - \sin(x) + u(t)$$

where $u(t) = \beta\sigma + \beta m \sin\Omega t + m\Omega\cos\Omega t$.

4.4.4 Comparing to the Damped Pendulum Model

It is often helpful to compare a models with more familiar ones. Consider the very well known damped pendulum model

$$ml^2\ddot{\theta} + bl^2\dot{\theta} + mgl\sin(\theta) = \tau_i\cos(\omega_i t)$$

where θ is the displacement angle, m the mass, l the length, g the gravitational constant, τ_i the driving input torque amplitude, and ω_i the input torque frequency.

Equation (4.6) is nearly equivalent, especially under the conditions $\beta = 2\zeta$, $\sigma = 0$. Furthermore, the local behavior of the homogeonous PLL is equivalent to that of the driven pendulum, since $\cos(2\pi n) = 1,\ n \in \mathbb{Z}$. It follows that the PLL dynamics is a superset of the damped pendulum dynamics. One can find a thorough exploration of the driven pendulum dynamics, including chaotic bifurcations, in several textbooks on nonlinear dynamics.

4.4.5 Fixed Points of the PLL

When $m = 0$, the PLL has fixed points for $y = 0$, and $\sin x = \beta\sigma$. Naturally, when $\beta\sigma > 1$ we have exceeded the phase detector's functional range, resulting in a steady-state frequency error. For small enough frequency detuning we eventually achieve a phase-lock, and the system will have fixed points at $(x, y) = \big(n\pi + (-1)^n \sin^{-1}(\beta\sigma), 0\big)$.

Analyzing the homogeneous equation, we get one class of periodically recurring equilibria when $\phi = 2\pi n + \pi,\ n \in \mathbb{Z}$. This class is always locally homeomorphic to a saddle point with eigenvalues $\lambda_{1,2} = \zeta - \beta \pm \sqrt{(\zeta - \beta)^2 + 1}$. Another class of periodically recurring equilibria at $\phi = 2\pi n,\ n \in \mathbb{Z}$, are locally homeomorphic to a linear system with eigenvalues of $\lambda_{1,2} = -\zeta \pm \sqrt{\zeta^2 - 1}$. Table 4.1 summarizes these local dynamics as a function of ζ.

Table 4.1: Locally Homeomorphic Bifurcations in ζ

Condition	Local Behavior to $\phi \approx 2\pi n$, $\dot{\phi} \approx 0$
$1 < \zeta$	stable node
$0 < \zeta < 1$	stable focus
$\zeta = 0$	center
$0 < \zeta < -1$	unstable focus
$\zeta < -1$	unstable node

4.4.6 Hamiltonian Parameterization

When $\zeta = \beta = 0$, equation 16 is a Hamiltonian system with

$$H(x, y) = y^2/2 - \cos x$$

Depending on the initial conditions provided, the Hamiltonian parameterization can produce several trajectories of interest including undamped oscillations around each stable equilibrium, heteroclinic orbits, and undamped cycle slips. These cases are shown in Figure 4.5 with the respective initial conditions, $(0, 1)$, $(-\pi + \epsilon, \epsilon)$, and $(-\pi, 1)$. This is exactly the same as an undamped pendulum, which has been extensively studied.

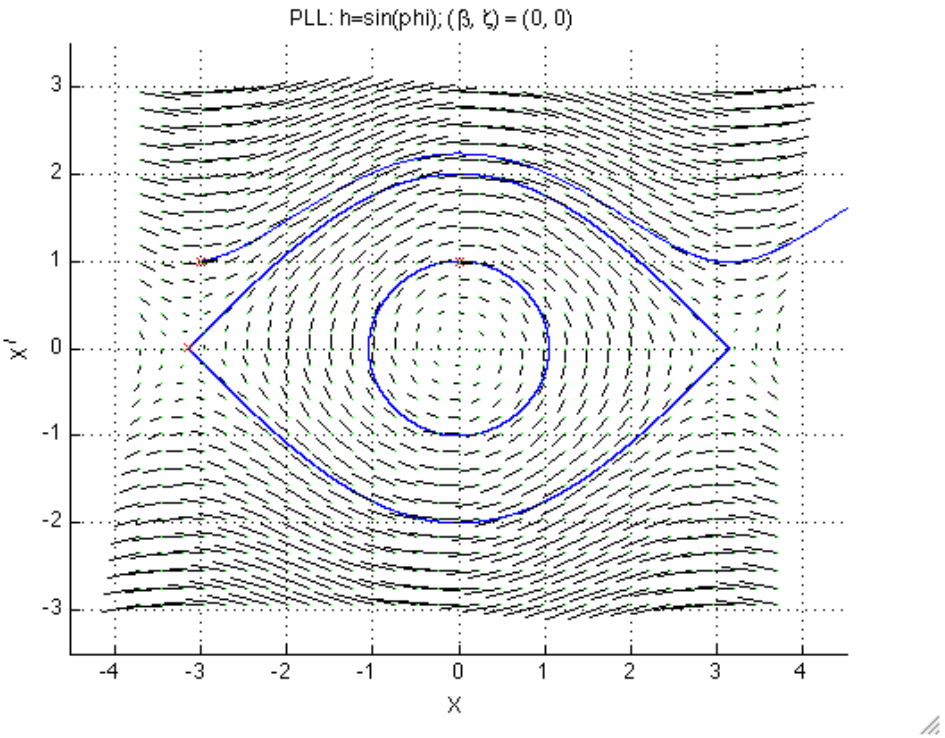

PLL with $\beta = \zeta = 0$

Figure 4.5: Phase-plane of Hamiltonian PLL

4.4.7 Exploring the Unmodulated Case

Ignoring the complication of phase-modulation by letting $m = 0$ in (4.6), we hope to explore the nonlinear dynamics of the second-order, type I PLL. The only nonlinearity is the use of an analog multiplier as a phase detector. When $\sigma \neq 0$, we are left with an input sinusoid with a fixed frequency ω_c that is not equal to the VCO natural frequency, ω_o.

To gain some intuition on how the parameters affect the dynamics, we perturb the system about the nominal parameterization, $\beta = 1,\ \zeta = 0.1,\ \sigma = 0$. Notice how the phase plots change with increasing β, ζ, and σ in Figures 29, 30, and 31 respectively. Note that except of one case, all of these phase plots have similar topology, alternating between saddles and stable foci.

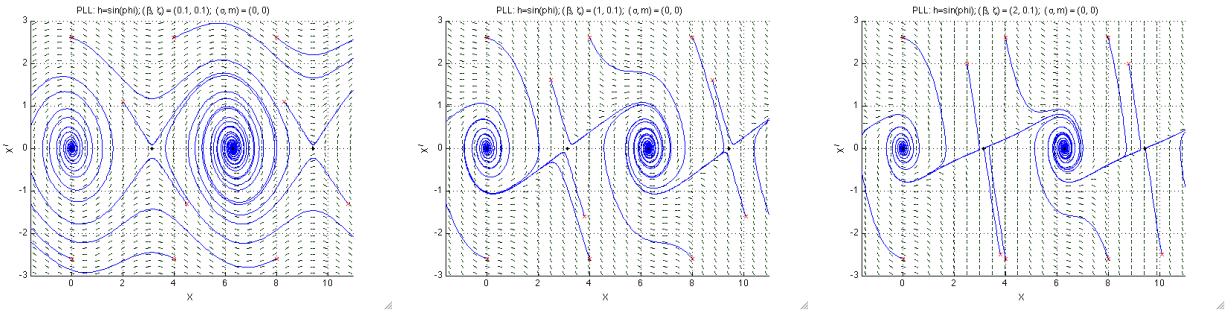

$\beta = 0.1,\ \zeta = 0.1$ $\beta = 1.0,\ \zeta = 0.1$ $\beta = 2.0,\ \zeta = 0.1$

Figure 4.6: Effects of increasing β

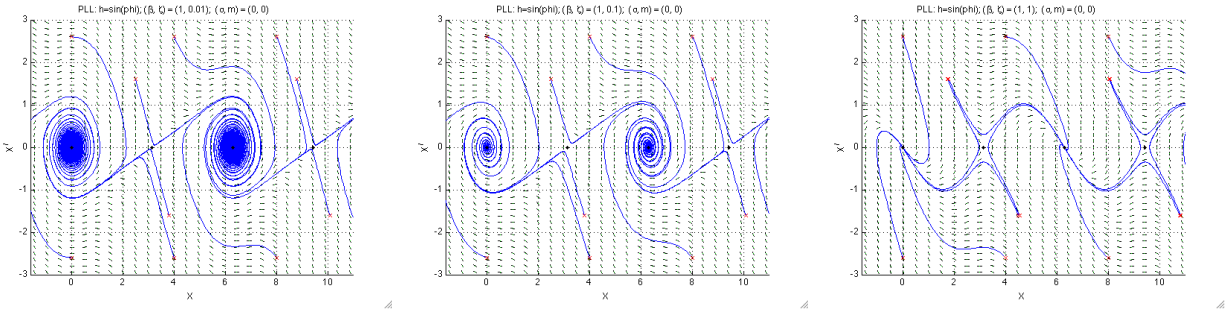

$\beta = 1.0,\ \zeta = 0.01$ $\beta = 1.0,\ \zeta = 0.1$ $\beta = 1.0,\ \zeta = 1.0$

Figure 4.7: Effects of increasing ζ

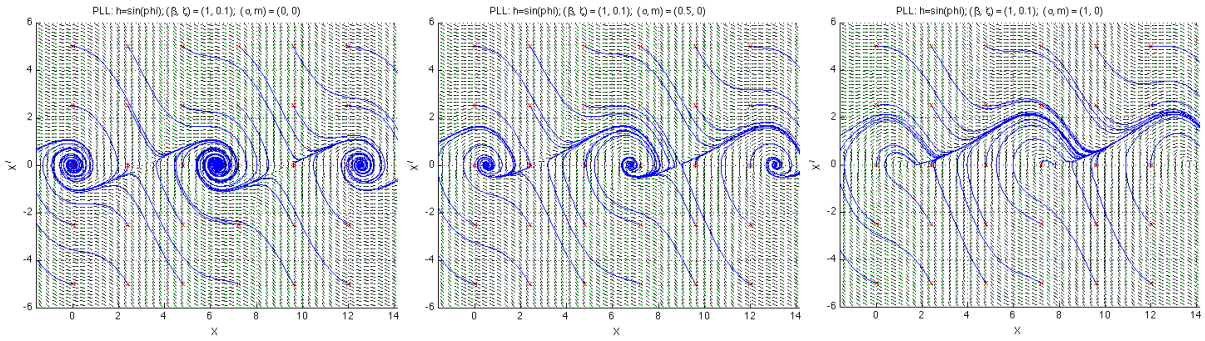

$\sigma = 0$ $\sigma = 0.5$ $\sigma = 1.0$

Figure 4.8: Effects of increasing σ with $\beta = 1$, $\zeta = 0.1$

Figure 4.6 shows that increasing β causes a rapid decay in angular velocity far from the equilibria, yet the oscillatory nature close to stable equilibria remains unchanged. Figure 4.7, as well as Table 4.1, demonstrate that increasing ζ reduces the oscillatory nature in the neighborhood of the stable equilibria. Finally, inclusion of an offset frequency reference, $\sigma \neq 0$, generally just

shifts the equilibria for small offsets. However, in the third graph of Figure 4.8, with $\beta = 1$, $\zeta = 0.1$, and $\sigma = 1$, the PLL is cycle slipping due to the analog multiplier's limited phase detection range.

4.4.8 Exploring the Modulated Case

In order to analyze the modulated input we utilize a Poincaré map sampled at the modulation frequency. Figure 4.9 shows three Poincaré maps (in black) with the initial condition $(0, \sqrt{\pi})$, and the parameters shown, when we modulate by 3, 4, and 7 times the natural angular frequency.

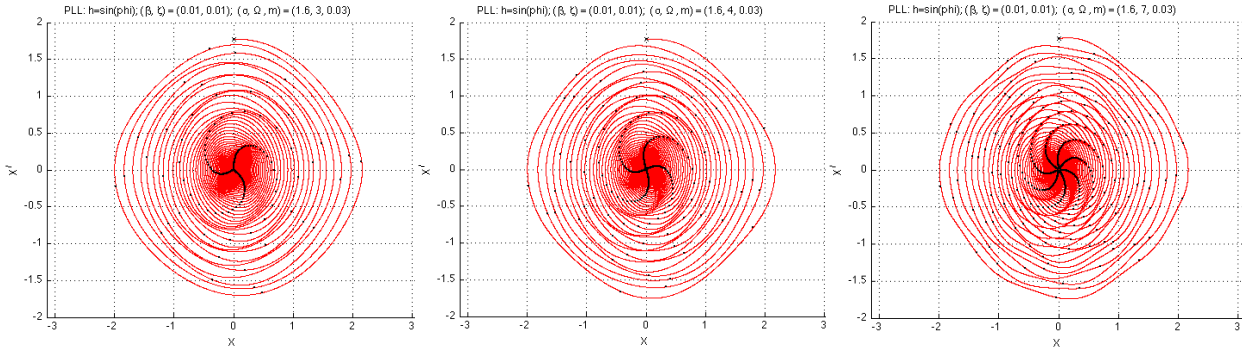

$\Omega = 3$ $\Omega = 4$ $\Omega = 7$

Figure 4.9: Effects of increasing Ω

Like a driven pendulum, high energy initial conditions and powerful driving forces result in more difficulty achieving equilibrium. Consider the modulated input case with $\Omega = 5$, and $m = 0.9$. In Figure 4.10a we show the Poincaré map of the transient response with the initial condition $(x(0), \dot{x}(0)) = (\pi, 0.98\sqrt{\pi})$. For these same Poincaré samples, only the first 2^{10}, In Figure 4.10b the zero-one test shows how divergent the transient response is. Naturally, the zero-one test makes a dramatic shift to the non-chaotic conclusion when more samples are used.

It is clear that nearby trajectories could result in periodic outputs with fixed phase differences, as the two trajectories may slip a different number of cycles. So, from a Lyapunov exponent point of view, nearby trajectories are not exponentially separated. Yet it is interesting that we do not

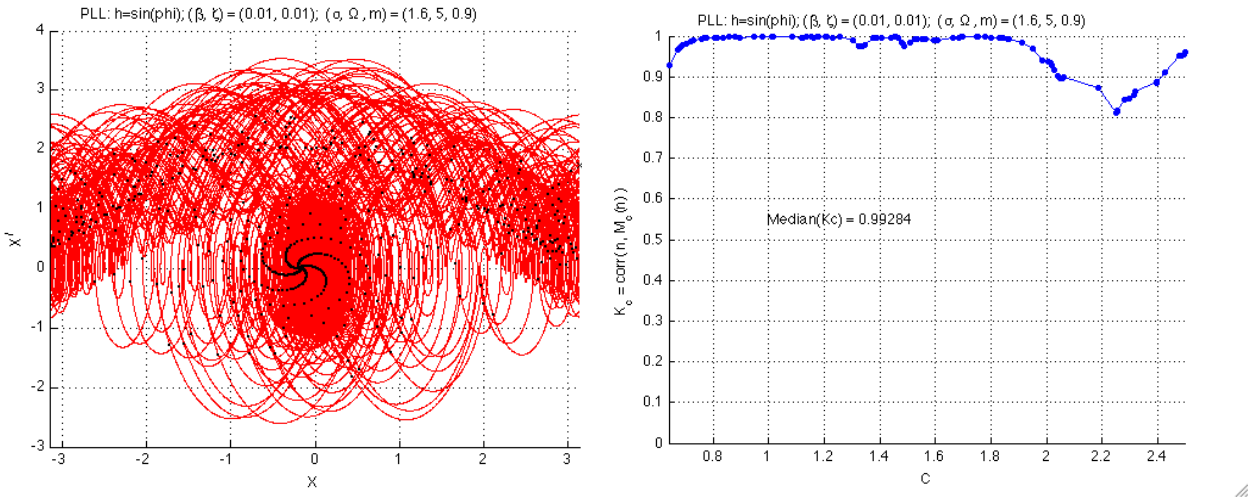

a) Poincaré Map

b) Zero-One Test

Figure 4.10: Transient Chaos

know deterministically how many cycles the system may slip because of the inherent sensitivity of the transient response.

4.4.9 PLL Conclusions

The PLL is a readily occurring dynamic system that helps explain how oscillating systems become entrained. We investigated the topology of PLLs and showed in a general sense how phase-detectors arise from the inherent nonlinearities of a system. Finally, we explored typical phase-lock dynamics, both linear and nonlinear. Many others have compiled relevant discussions of PLL dynamics, including the famous damped pendulum dynamics[16][17] or the use of Melinkov's method to explore the onset of choas in the PLL[15]. Bradley[18] exploits the chaotic capability of the PLL to broaden the capture range. Liu[19] designs a controller that controls the rich bifurcations using two parameters.

4.5 Conclusions

Oscillators are dynamic systems that typically produce periodic orbits, quasi-periodic orbits, or limit cycles. By characterizing the narrow space of linear oscillators we have concluded that most autonomous oscillators are inherently nonlinear systems. The specific oscillators studied in this research conform to Liénard's equation. The Poincaré-Bendixson theorem provides a surprisingly general criteria for the existence of periodic orbits in second-order, continuous, dynamical systems; while Liénard's theorem provides intuitive criteria for a narrower class of practical, second-order oscillators.

We focus on characterizing Duffing dynamics, which has four fundamental modes of operation arising from a pitchfork well in the spring constant, α, and a hyperbolic well in the nonlinear stiffening coefficient, β. We demonstrate that periodically forcing a Hamiltonian parameterization of the Duffing equation produces quasi-periodic and chaotic trajectories. The chaotic trajectories are quite useful in discovering neighboring quasi-period modes of operation. We put the 0-1 test to use. Although Romero-Bastida[5] reported difficulties with a couple of Hamiltonian systems, our

use of the test found results consistent with expectations from current literature.

The Van der Pol oscillator is characteristic of many engineered oscillators and has a rich academic history. It satisfies the Liénard's theorem by destabilized origin while maintaining global stability with a nonlinear damping function, resulting in a limit-cycle. We notice that the forced Van der Pol equation produces a lot of nonlinear effects. We reference some of the bifurcation studies done on this oscillator.

Finally, the phenomena of synchronization is explored using the phase-locked loop. The topology of the phase model is presented and a practical linear example is demonstrated. The nonlinear dynamics are then explored for a second-order PLL using a lead-lag filter. We discuss the local behavior of the fixed points and show that the Hamiltonian parameterization is simply an undamped pendulum. Finally, the unmodulated and modulated dynamics are simulated. We notice that the transient dynamics are quite unpredictable when the PLL is given high energy initial conditions.

Bibliography

[1] P. J. P. J. R. Dormand, "A family of embedded runge-kutta formulae," Jour. of Comp. and Applied Math., vol. 6, pp. 19–26, 1980.

[2] J. D. Meiss, Differential Dynamical Systems. Philadelphia: SIAM, 2007.

[3] H. K. Khalil, Nonlinear Systems, 3rd ed. U.S.A.: Prentice Hall, 2002.

[4] L. Barreira, "Poincaré recurrence: old and new," XIVth Intl. Congress on Mathl. Phys, pp. 415–422, 2006.

[5] B. Romero-Bastida, Olivares-Robles, "Probing hamiltonian dynamics by means of the 0-1 test for chaos," Journal of Physics A, vol. 42, 2009.

[6] G. A. Gottwald and I. Melbourne, "On the implementation of the 0-1 test for chaos," SIAM J Applied Dyn Sys, vol. 8, pp. 129–145, 2009.

[7] M. Cartwright, "Balthazar van der pol," J. London Math Soc., pp. 367–376, 1960.

[8] Ueda and N. Akamatsu, "Chaotically transitional phenomena in the forced negative resistance oscillator," IEEE Trans. Circ. and Sys., vol. 28, pp. 217–224, 1981.

[9] N. Inaba, "Chaos via torus breakdown in the forced van der pol oscillator," IEEE Trans. on Circuits and Systems, vol. 2, pp. 1051–1054, 1990.

[10] Bennet, "Huygens clocks," Proc. R. Soc. London, vol. 458, pp. 563–579, 2002.

[11] F. M. Gardner, Phaselock Techniques, 3rd ed. New Jersey: Wiley, 2008.

[12] R. E. Best, Phase-Locked Loops, 6th ed. U.S.A.: McGraw Hill, 2007.

[13] A. Suarez, Autonomous Microwave Circuits. Wiley, 2009.

[14] E. Rubiola, Phase Noise and Frequency Stability in Oscillators, 1st ed. Cambridge: Cambridge University Press, 2009.

[15] T. Endo and L. O. Chua, "Chaos from phase-locked loops," IEEE Transactions on Circuits and Systems, vol. 35, no. 8, pp. 987–1003, 1988.

[16] F. C. Moon, Chaotic and Fractal Dynamics. Germany: Wiley-Vch, 2004.

[17] J. Stensby, "Saddle node bifurcation in a pll," Southeastcon '93, Proc. IEEE, no. 5003886, p. 4, 1993.

[18] E. Bradley, "Using chaos to broaden the capture range of a phase-locked loop," IEEE Transactions on Circuits and Systems, vol. 40, no. 11, pp. 808–818, 1993.

[19] e. Z. F. Liu, "Controlling chaos in phase-locked loop," IECON '98 Proc 24th Conf. of the IEEE, vol. 3, pp. 1560–1563, 1998.